Allosteric activation or inhibition of PI3Kγ mediated through conformational changes in the p110γ helical domain

Noah J Harris[1*], Meredith L Jenkins[1*], Sung-Eun Nam[2] Manoj K Rathinaswamy[1], Matthew AH Parson[1], Harish Ranga-Prasad[1], Udit Dalwadi[2], Brandon E Moeller[1], Eleanor Sheekey[1], Scott D Hansen[3], Calvin K Yip[2%], and John E Burke[1,2%]

[1]Department of Biochemistry and Microbiology, University of Victoria, Victoria, British Columbia, V8W 2Y2, Canada

[2]Department of Biochemistry and Molecular Biology, The University of British Columbia, Vancouver, British Columbia V6T 1Z3, Canada

[3]Department of Chemistry and Biochemistry, Institute of Molecular Biology, University of Oregon, Eugene, OR 97403

*These authors contributed equally

[%]To whom correspondence should be addressed: John E. Burke

Tel: 1-250-721-8732, email: jeburke@uvic.ca

Calvin K. Yip

Tel: 1-604-827-3976, email: calvin.yip@ubc.ca

Keywords: PI3K, PIK3CG, PI3Kγ, p110γ, p101, p84, PIK3R5, PIK3R6, phosphoinositide 3-kinase, hydrogen exchange, protein kinase C, PKC, nanobodies.

Abstract

PI3Kγ is a critical immune signaling enzyme activated downstream of diverse cell surface molecules, including Ras, PKCβ activated by the IgE receptor, and Gβγ subunits released from activated GPCRs. PI3Kγ can form two distinct complexes, with the p110γ catalytic subunit binding to either a p101 or p84 regulatory subunit, with these complexes being differentially activated by upstream stimuli. Here using a combination of Cryo electron microscopy, HDX-MS, and biochemical assays we have identified novel roles of the helical domain of p110γ in regulating lipid kinase activity of distinct PI3Kγ complexes. We defined the molecular basis for how an allosteric inhibitory nanobody potently inhibits kinase activity through rigidifying the helical domain and regulatory motif of the kinase domain. The nanobody did not block either p110γ membrane recruitment or Ras/Gβγ binding, but instead decreased ATP turnover. We also identified that p110γ can be activated by dual PKCβ helical domain phosphorylation leading to partial unfolding of an N-terminal region of the helical domain. PKCβ phosphorylation is selective for p110γ-p84 compared to p110γ-p101, driven by differential dynamics of the helical domain of these different complexes. Nanobody binding prevented PKCβ mediated phosphorylation. Overall, this works shows an unexpected allosteric regulatory role of the helical domain of p110γ that is distinct between p110γ-p84 and p110γ-p101, and reveals how this can be modulated by either phosphorylation or allosteric inhibitory binding partners. This opens possibilities of future allosteric inhibitor development for therapeutic intervention.

Introduction

The class I phosphoinositide 3 kinases (PI3Ks) are master regulators of myriad functions through their generation of the lipid signalling molecule phosphatidylinositol 3,4,5-trisphosphate (PIP_3) downstream of cell surface receptors (Burke and Williams, 2015; Rathinaswamy and Burke, 2019; Vanhaesebroeck et al., 2021; Vasan and Cantley, 2022). The class I PI3Ks can be further subdivided into the class IA and class IB subfamilies, with class IB PI3Ks being critical in immune signalling, and are composed of a single p110γ catalytic subunit that can bind to either a p101 or p84 regulatory subunit (Hawkins and Stephens, 2015; Lanahan et al., 2022; Okkenhaug, 2013). The two PI3Kγ complexes (either p110γ-p84 or p110γ-p101) play essential and independent roles in both the adaptative and innate immune systems. PI3Kγ has shown promise as a therapeutic target, primarily as an immunomodulator of the tumor microenvironment leading to enhanced anti-tumor immune responses (De Henau et al., 2016; Kaneda et al., 2016b). Multiple isoform selective small molecule ATP competitive inhibitors of p110γ are in clinical trials for multiple forms of human cancers (Li et al., 2021). However, all inhibitors currently developed towards p110γ act as ATP competitive inhibitors, showing equal potency against both p110γ-p84 or p110γ-p101 complexes.

Detailed experiments on the role of p110γ in mice show that knockout of both p101 and p84 leads to PIP_3 levels that are equivalent to knockout of p110γ, showing that all cellular PI3Kγ activity requires the presence of either a p84 or p101 regulatory subunit (Rynkiewicz et al., 2020). The two complexes are differentially activated by membrane localised receptors, including G-protein coupled receptors (Li et al., 2000; Stephens et al., 1997), Ras (Jin et al., 2020; Kurig et al., 2009), toll like receptors (TLRs) (Luo et al., 2018), and the IgE antigen receptor (Laffargue et al., 2002; Walser et al., 2013). This leads to the different complexes driving unique immune responses, with p110γ-p101involved in chemotaxis in neutrophils (Bohnacker et al., 2009; Deladeriere et al., 2015), and p110γ-p84 involved in reactive oxide production. Differential activation of unique PI3Kγ complexes downstream of GPCRs and Ras is caused by the ability of p101 to directly bind to Gβγ subunits downstream of activated GPCRs, with this being lost in

81 p84, making p110γ-p84 activation by Gβγ dependent on Ras mediated membrane
82 recruitment (Rathinaswamy et al., 2023; Kurig et al., 2009; Rynkiewicz et al., 2020).
83 Activation of PI3Kγ downstream of the IgE antigen receptor is driven by calcium mediated
84 activation of protein kinase Cβ, leading to the selective phosphorylation and activation of
85 p110γ at S582 (Walser et al., 2013), with this putatively only occurring in p110γ-p84 and
86 not p110γ-p101. The full molecular mechanisms underlying how phosphorylation of p110γ
87 is selective for different p84 or p101 complexes, and how it activates lipid kinase activity
88 are poorly understood.

89 Extensive biophysical approaches including cryo electron microscopy (cryo-EM),
90 X-ray crystallography, and hydrogen deuterium exchange mass spectrometry (HDX-MS)
91 have provided extensive insight into the molecular underpinnings of how p110γ
92 associates with both p101 and p84, how they are differentially activated by Ras and
93 GPCR signals, and how they can be activated on lipid membranes (Pacold et al., 2000;
94 Walker et al., 1999; Rathinaswamy et al., 2021c, 2021a; Gangadhara et al., 2019; Vadas
95 et al., 2013; Rathinaswamy et al., 2023). The p110γ catalytic subunit is composed of an
96 adaptor binding domain (ABD), a Ras binding domain (RBD), a C2 domain, a helical
97 domain, and a bi-lobal kinase domain (Rathinaswamy et al., 2021a; Walker et al., 1999).
98 A set of helices positioned C-terminal to the activation loop in the kinase domain play a
99 critical role in regulating activity, with this region referred to as the regulatory motif
100 (Rathinaswamy et al., 2021c). The p110γ isoform is unique in that it is inhibited in the
101 absence of a regulatory subunit, with this driven by an autoinhibitory conformation of the
102 regulatory motif, that is proposed to require membrane association to disrupt
103 (Gangadhara et al., 2019). The regulatory motif is a common site of activating mutations
104 in the other class I PI3K isoforms (Jenkins et al., 2023), with p110γ having rare activating
105 oncogenic mutants in this region (Rathinaswamy et al., 2021c). The p110γ subunit
106 interacts with both p84 and p101 at an interface composed of the C2 domain, and the
107 linkers between the RBD-C2 and C2-helical domains (Rathinaswamy et al., 2023, 2021a).
108 The p110γ-p84 complex forms a more dynamic complex compared to p110γ-p101
109 (Rathinaswamy et al., 2023; Shymanets et al., 2013), however, no clear unique regulatory
110 role of this difference in dynamics has been identified.

111 The fundamental roles of p110γ in inflammatory processes has made it a
112 therapeutic target in many pathological conditions, including asthma (Campa et al., 2018),
113 arthritis (Camps et al., 2005), obesity (Becattini et al., 2011; Breasson et al., 2017), and
114 cancer (De Henau et al., 2016; Kaneda et al., 2016a, 2016b). There are significant side
115 effects from non-isoform selective PI3K inhibitors (Bohnacker et al., 2017;
116 Vanhaesebroeck et al., 2021), which has driven the development of highly p110γ selective
117 small molecule inhibitors (Bell et al., 2012; Evans et al., 2016; Gangadhara et al., 2019).
118 However, all p110γ inhibitors will target both p110γ-p101 and p110γ-p84, so there is a
119 potential for the development of allosteric inhibitors outside of the ATP binding site. Initial
120 promise has been reported for the development of class IA p110α oncogene specific
121 allosteric inhibitors. However, further investigation of the molecular mechanisms
122 underlying p110γ regulation will be required for the discovery of regions that can be
123 targeted for allosteric inhibitor development.
124 Here we report critical roles of the helical domain of p110γ in both activation and
125 inhibition of lipid kinase activity. We characterised an allosteric inhibitory nanobody (NB7)
126 that potently inhibits p110γ activity. Cryo-EM was used to define the inhibitory interface,
127 which is composed of the helical domain, the ABD-RBD linker, and the regulatory motif
128 of the kinase domain of p110γ. The region that the nanobody binds to is in close spatial
129 proximity to a previously identified PKCβ phosphorylation site (S582) in the helical
130 domain, and oncogenic activating mutants in the regulatory motif. We fully characterised
131 the activity and dynamics of stoichiometrically PKCβ phosphorylated p110γ, leading to
132 the discovery of a novel additional phosphorylation site (S594/S595). PKCβ
133 phosphorylation was highly selective for p110γ and p110γ-p84, with limited
134 phosphorylation of p110γ-p101. Hydrogen deuterium exchange mass spectrometry
135 (HDX-MS) analysis showed that phosphorylation of p110γ leads to unfolding of the N-
136 terminal region of the helical domain, and increased kinase activity. The presence of the
137 inhibitory nanobody significantly blocks PKCβ phosphorylation, with phosphorylated
138 p110γ showing no detectable binding to NB7. Overall, this work provides unique insight
139 into the critical role of the helical domain in controlling p110γ activity, and how

140 phosphorylation and binding partners can modify this regulation. It also reveals a unique
141 binding site located at the interface of the helical and kinase domain that can be targeted
142 for future allosteric inhibitor design.
143
144 **Results**
145 *Molecular mechanism of nanobody inhibition of p110γ*
146 We previously identified multiple nanobodies that inhibited the activity of p110γ.
147 One from this group (denoted NB7 throughout the manuscript) potently inhibited the
148 membrane mediated activation of p110γ-p84 by both Ras and Gβγ, with HDX-MS
149 experiments mapping the NB7 binding interface to the RBD, helical and kinase domains
150 (Rathinaswamy et al., 2021b). We originally hypothesized that NB7 worked by sterically
151 inhibiting Ras binding to the RBD domain of p110γ. To further explore the molecular
152 mechanism of inhibition we purified all complexes of p110γ (p110γ apo, p110γ-p84,
153 p110γ-p101) along with the NB7 nanobody. The SDS-PAGE of all proteins utilised in this
154 study are shown in the source data file included in the supplemental information.
155 To define the mechanism concerning how NB7 inhibits PI3K activity we analyzed
156 how this nanobody inhibited all class IB PI3K complexes (p110γ, p110γ-p84, p110γ-p101)
157 upon activation by lipidated Gβγ subunits. Intriguingly, we found that all three forms of
158 p110γ were potently inhibited by NB7 (Fig. 1A). While the IC_{50} measured for the three
159 complexes was different, this is likely mainly due to the dramatic difference in protein
160 required to measure lipid kinase activity *in vitro* (~300 nM for p110γ apo/p110γ-p84, and
161 ~10 nM for p110γ-p101, respectively). This suggested that the mechanism of inhibition
162 was not driven by a steric block of Ras association through the RBD, as previously
163 proposed (Rathinaswamy et al., 2021b). We examined the binding of this nanobody to all
164 complexes using biolayer interferometry (BLI). The nanobody bound equivalently tightly
165 to all complexes, with ~2 nM potency for p110γ, p110γ-p84, and p110γ-p101 (Fig. 1B).
166 We also tested binding of the nanobody to all class IA PI3Ks, and there was no detectable
167 binding to p110α, p110β, and p110δ (Fig. 1C).

168 To further understand the mechanism by which this nanobody blocked lipid kinase
169 activity we measured the bulk membrane recruitment dynamics of fluorescently labeled
170 Dy647-p84-p110γ on supported lipid bilayers (SLBs) using Total Internal Reflection
171 Fluorescence (TIRF) Microscopy. We found that the nanobody had no effect on
172 membrane recruitment of p110γ-p84 on bilayers containing membrane-tethered
173 Ras(GTP) and Gβγ (Fig. 1D-F). Membrane binding was not affected when the nanobody
174 was spiked into samples containing membrane associated Dy647-p84-p110γ (Fig 1D).
175 Similarly, pre-incubation of Dy647-p84-p110γ with 500 nM NB7 did not perturb membrane
176 association of the kinase when flowed over a supported membrane (Fig. 1E).
177 We wanted to define the molecular mechanism of how nanobody NB7 was a potent
178 allosteric inhibitor of lipid kinase activity. We purified the complex of nanobody NB7 bound
179 to p110γ-p84 to homogeneity by gel filtration. Using this sample, we obtained a cryo-EM
180 reconstruction of the complex of nanobody (NB7)-bound p110γ at 3.0-Å overall resolution
181 from 149,603 particles (Figs. 2A-D, S1 and supplemental table 1). The density map was
182 of sufficient quality to perform automated and manual construction of the p110γ-NB7
183 complex, with unambiguous building of the interfacial contacts between NB7 and p110γ.
184 Nanobody binding did not induce any large-scale conformational changes of p110γ, as
185 the structure of p110γ bound to NB7 was similar to the apo p110γ crystal structure or
186 p110γ-p101 cryo-EM structure (Fig. S2). The lowest local resolution was in the ABD
187 domain, with increased B-factors of the ABD in the p110γ-NB7 structure compared to
188 p110γ-p101 (Fig. S2). This is consistent with the concept that ABD flexibility plays an
189 important role in class I PI3K regulation (Liu et al., 2022).
190 The interface between NB7 and p110γ was extensive, with ~1200 Å of buried
191 surface area, with interactions of the ABD-RBD linker, N-terminus of the helical domain,
192 and the regulatory motif at the turn between kα8-kα9 (1022-1026aa). This location in the
193 regulatory motif is where both activating oncogenic (R1021C) and inhibitory loss of
194 function mutants have been identified (R1021P) (Takeda et al., 2019), as well as a
195 putative inhibitory phosphorylation site (T1024) (Perino et al., 2011). The resolution was
196 sufficient to unambiguous build the three complementarity determining region (CDR)

197 loops of NB7 that mediate target selectivity (Fig. 2E-F). The interface is primarily
198 hydrophobic, with only 8 hydrogen bonds, and 1 electrostatic interaction among the 33
199 interfacial residues of NB7. A pocket formed between the helical domain and the ABD-
200 RBD linker forms the majority of the interface, with extensive interactions with the long
201 CDR3. The CDR1 loop packed up against the N-terminal section of the helical domain,
202 with the CDR2 loop forming the interface with the regulatory motif. Previous study of
203 oncogenic mutants in the regulatory motif of p110γ showed that increased dynamics
204 mediated by these mutants increased kinase activity, putatively by breaking the
205 autoinhibitory tryptophan lock in kα12 of the regulatory motif. Therefore, rigidifying the
206 regulatory motif likely explains the molecular basis for how it prevents kinase activity. The
207 nanobody interface is distinct from the predicted Gβγ interface (Rathinaswamy et al.,
208 2023) and the experimentally resolved Ras interface (Pacold et al., 2000), explaining why
209 it can still be membrane recruited by these stimuli.
210
211 *p110γ activation by helical domain phosphorylation*
212 To further understand the potential role helical domain dynamics in regulating
213 p110γ activity we searched for any possible regulatory roles of this in PI3K signalling. It
214 has been previously identified that p110γ is directly phosphorylated by the protein kinase
215 PKCβ on residue S582 in the helical domain (Walser et al., 2013). S582 is located on the
216 interior of the helical domain, and would not be expected to be exposed when the N-
217 terminal region of the helical domain is folded (Fig. 3A). To understand this better at a
218 molecular level, we purified a catalytic fragment of PKCβ and performed protein
219 phosphorylation reactions on p110γ apo, p110γ-p84, and p110γ-p101. We identified a
220 phosphorylated peptide containing S582, and surprisingly, we found an additional p110γ
221 phosphorylation site at S594/S595 (Fig. 3B, Fig. S3). The S594/S595 site is also located
222 in the N-terminal region of the helical domain, and is even more buried than S582, and
223 would not be expected to be exposed when this region is folded (Fig. 3A). Dose response
224 curves of PKCβ treatment were carried out for p110γ (Fig. 3C), p110γ-p84 (Fig. 3D), and
225 p110γ-p101 (Fig. 3E). Both p110γ and p110γ-p84 showed similar dose response curves

226 for PKCβ treatment, with similar curves for S582 and S594/S595. The p110γ-p101
227 complex was only very weakly phosphorylated, with <100-fold lower levels compared to
228 p110γ and p110γ-p84 (Fig. 3E). This is consistent with the helical domain in p110γ being
229 more rigid when bound to p101, compared to either bound to p84 or p110γ alone.

230 To provide additional insight into the molecular mechanisms underlying p110γ
231 phosphorylation we carried out hydrogen deuterium exchange mass spectrometry (HDX-
232 MS) experiments on p110γ and phosphorylated p110γ (90.8% phosphorylated S594/595,
233 92% phosphorylated S582) (Fig. 4A). The full data underlying the experiment is available
234 in the source data, and data processing information is in supplemental table 2. We have
235 previously observed that the N-terminal region of the helical domain of apo p110γ
236 (residues spanning 557-630aa) shows isotope profiles that are consistent with EX1 H/D
237 exchange kinetics (Rathinaswamy et al., 2021b, 2021c; Vadas et al., 2013; Walser et al.,
238 2013). This is indicative of cooperative unfolding of extended protein regions, with H/D
239 exchange occurring faster than the refolding event. This region is where the PKC
240 phosphorylation sites are located, and may explain how the buried residues S582 and
241 S594/S595 can be exposed to PKC. This is compatible with the observation that p110γ-
242 p101 is protected from phosphorylation, as it does not show EX1 kinetics in this region,
243 whereas both p110γ and p110γ-p84 do (Rathinaswamy et al., 2021a).

244 When we compared phosphorylated p110γ (>90.8% as measured by mass
245 spectrometry at both sites) to unphosphorylated p110γ we observed extensive increases
246 in dynamics in the C2, helical domain and kinase domain (Fig. 4A-D). The largest
247 increases in exchange upon phosphorylation were located in the N-terminal region of the
248 helical domain, with the peptides directly adjacent to the phosphorylation site showing
249 almost complete deuterium incorporation at the earliest time points of exchange. This is
250 indicative of significant disruption of the alpha helical secondary structure in this region.
251 When we examined the exchange profiles in this region they still underwent EX1 kinetics
252 (Fig. 4C), however, phosphorylated p110γ was enriched in the more fully deuterated
253 species. In addition to the regions in the helical domain, a portion of the regulatory motif
254 of the kinase domain also showed increased deuterium exposure. This included the kα9-

255 kα12 helices that surround the activation loop of p110γ. These increases in exchange
256 were similar to those we had observed in a R1021C oncogenic activating mutant of
257 *PIK3CG* (Rathinaswamy et al., 2021c).

258 To further explore the potential role of phosphorylation in mediating p110γ activity,
259 we examined the kinase activity of p110γ for both basal ATPase and lipid membranes.
260 Assays measured the hydrolysis of ATP to ADP, with this acting as a surrogate for PIP_3
261 production in the membrane assay. PKCβ-mediated phosphorylation enhanced the
262 ATPase activity of p110γ ~2-fold in both the absence and presence of membranes (Fig.
263 4E).

264

265 *Nanobody blocks p110γ phosphorylation*

266 As NB7 bound at the interface of the helical and kinase domains that is exposed
267 upon PKC phosphorylation of p110γ we hypothesized that the nanobody would likely alter
268 phosphorylation. We carried out PKC phosphorylation of p110γ, p110γ-p101 and p110γ
269 bound to NB7. The presence of NB7 showed even lower phosphorylation than p110γ-
270 p101, with almost complete abrogation of phosphorylation at both sites (Fig. 5A-B). We
271 also wanted to determine whether p110γ phosphorylation reciprocally perturbed NB7
272 binding. BLI experiments showed that there was no detectable binding of NB7 to
273 phosphorylated p110γ (Fig. 5C-D), consistent with phosphorylation disrupting the N-
274 terminal region of the p110γ helical domain. In addition, lipid kinase assays using
275 phosphorylated p110γ showed no detectable difference in activity when measured in the
276 absence and presence nanobody (Fig. 5E).

277

278 **Discussion**

279 Here we find that the helical domain is a central regulator of the p110γ catalytic
280 subunit of class IB PI3K, with modulation of helical dynamics through binding partners or
281 PTMs able to either increase or decrease lipid kinase activity. These results expand on
282 previous work defining the helical domain as a central regulator of class IA PI3Ks, where
283 the nSH2 domain of the p85 regulatory subunits makes inhibitory interactions that

284 significantly inhibit lipid kinase activity of all class IA catalytic subunits (p110α, p110β,
285 and p110δ) (Mandelker et al., 2009; Miled et al., 2007; Burke and Williams, 2013; Burke,
286 2018). This inhibitory interaction in class IA PI3Ks is disrupted in human cancers (helical
287 hotspot mutations in *PIK3CA*) (Samuels et al., 2004) and immune disorders (helical
288 mutations in *PIK3CD* in APDS1) (Angulo et al., 2013; Lucas et al., 2014). Class IB PI3Ks
289 are unique compared to class IA PI3Ks, as they are not inhibited by p101 and p84
290 regulatory subunits, but instead potentiate GPCR activation. This lack of inhibition is due
291 to the distinct binding interface of class IB PI3K regulatory subunits compared to class IA
292 regulatory subunits, with only class IA regulatory subunits making direct inhibitory
293 interactions with the kinase and helical domains of p110 catalytic subunits
294 (Rathinaswamy et al., 2021a). Here we show that a unique surface at the interface of the
295 helical and kinase domains of p110γ is a potential site for the development of novel
296 allosteric inhibitors that modulate p110γ activity.

297 The previously identified inhibitory nanobody (NB7) (Rathinaswamy et al., 2021b)
298 bound with high affinity and inhibited all complexes of p110γ. The nanobody interface is
299 distinct from how the nSH2 inhibits class IA PI3K activity, as its binding site is on the
300 opposite face of the helical domain (Fig. 6A). The mechanism of inhibition is also distinct,
301 as the nSH2-helical interaction plays a critical role in preventing membrane recruitment
302 of inhibited class I PI3Ks, with removal of this interface either through pYXXM motif
303 binding, or oncogenic mutations leading to increased membrane recruitment (Burke et
304 al., 2012, 2011; Zhang et al., 2011). Analysis of the nanobody binding site compared to
305 the structure of HRas-p110γ or the HDX-MS supported Alphafold-multimer prediction of
306 Gβγ-p110γ (Rathinaswamy et al., 2023) shows that nanobody binding does not sterically
307 block complex formation (Fig. 6B). This is consistent with it not blocking membrane
308 recruitment by Ras/Gβγ.The nanobody inhibited ATP turnover both in solution and on
309 membranes, suggesting that it prevents formation of a catalytically competent
310 conformation of p110γ, but still allows for membrane recruitment. Further development of
311 small molecule allosteric binding partners in this allosteric pocket between the kinase and
312 helical domain may reveal the specific molecular interactions in this pocket that mediate
313 inhibition.

314 Oncogenic mutations are frequent in the class IA PI3Kα encoded by *PIK3CA*, with
315 this being the 2nd most frequently mutated gene in human cancer (Lawrence et al., 2014).
316 Mutations in p110γ encoded by *PIK3CG* in cancer are less frequent, however, they can
317 still provide insight into regulatory mechanisms that control activity. Oncogenic mutations
318 in the kinase domain (R1021C) and helical domain (E581K) are in close proximity to the
319 nanobody binding site, and both would be expected to disrupt the stability of the helical
320 domain or regulatory motif of the kinase domain (Fig. 6C). In addition to these mutations
321 there are also multiple post-translational modifications that occur in this region, including
322 inhibitory phosphorylation at T1024 (Perino et al., 2011), and activating phosphorylation
323 at S582 (Walser et al., 2013). PKCβ is activated downstream of the IgE receptor in mast
324 cells (Walser et al., 2013), but the full details of how this activates PI3K has been unclear.
325 We identified an additional PKCβ phosphorylation site located in the helical domain
326 (S594/S595) (Fig. 6C). Both the S582 and S594/S595 sites are not surface accessible
327 and would require a transient opening of the helical domain for kinase accessibility. HDX-
328 MS analysis of the helical domain of p110γ has shown that it is more dynamic than other
329 class I PI3K isoforms (Burke and Williams, 2013; Walser et al., 2013), with the presence
330 of the p101 regulatory subunit dramatically decreasing helical domain dynamics (Vadas
331 et al., 2013). This putative mechanism of helical domain dynamics driving PKCβ
332 phosphorylation is consistent with our observation that p101 subunits decreased p110γ
333 phosphorylation >100-fold. PKCβ phosphorylation of p110γ leads to increased dynamics
334 in both the helical and kinase domains with increased kinase activity, although only
335 weakly compared to full activation by either membrane localised Ras or Gβγ. This
336 increase was observed with both membrane and soluble substrate, so likely is not driven
337 by altered membrane recruitment.
338 Overall, our biophysical and biochemical analysis of modulators of helical domain
339 dynamics reveal the critical role of this domain in regulating class IB PI3K activity. This
340 raises possibilities for development of small molecule modulators that may either increase
341 or decrease helical domain dynamics, leading to either activation or inhibition. The high-
342 resolution structure of an allosteric inhibitor nanobody provide initial insight into which
343 pockets can specifically be targeted. Multiple ATP competitive p110γ selective inhibitors

344 are in clinical trials for human cancers (Li et al., 2021), with many having significant side
345 effects. The identification of novel inhibitory strategies provides new opportunities for
346 targeting p110γ dysregulation in human disease.
347

348 **Acknowledgements**

349 J.E.B. is supported by the Canadian Institute of Health Research (CIHR, 168998),
350 and the Michael Smith Foundation for Health Research (MSFHR, scholar 17686). C.K.Y.
351 is supported by CIHR (FDN-143228, PJT-168907) and the Natural Sciences and
352 Engineering Research Council of Canada (RGPIN-2018-03951). S.D.H. is supported by
353 an NSF CAREER Award (MCB-2048060). This research project was supported in part by
354 the UBC High Resolution Macromolecular Cryo-Electron Microscopy Facility (HRMEM).
355 A portion of this research was supported by NIH grant U24GM129547 and performed at
356 the PNCC at OHSU and accessed through EMSL (grid.436923.9), a DOE Office of
357 Science User Facility sponsored by the Office of Biological and Environmental Research.
358 We appreciate help from Theo Humphreys and Rose Marie Haynes with data collection
359 at PNCC. Competing Interests: The authors declare that they have no competing
360 interests.
361

362 **Conflict of Interest statement**

363 JEB reports personal fees from Scorpion Therapeutics, Reactive therapeutics and
364 Olema Oncology; and research grants from Novartis. Other authors declare no competing
365 interests.
366

367 **Methods**

Resources table	SOURCE	IDENTIFIER
Bacterial and virus strains		
E.coli XL10-GOLD KanR Ultracompetent Cells	Agilent	200317
E.coli DH10EMBacY Competent Cells	Geneva Biotech	DH10EMBacY
Chemicals, peptides, and recombinant proteins		
Deuterium Oxide 99.9%	Sigma	151882
Guanosine 5′-diphosphate (GDP) sodium salt hydrate	Sigma	G7127-100MG
Guanosine 5′-triphosphate (GTP) sodium salt hydrate	Sigma	G8877-250MG
Sodium deoxycholate	Sigma	D6750

Polyoxyethylene (10) lauryl ether	Sigma	P9769
CHAPS, Molecular Biology Grade	EMD Millipore	220201
Phosphatidylserine (Porcine Brain)	Avanti	840032C
Phosphatidylethanolamine (Egg yolk)	Sigma	P6386
Cholesterol	Sigma	47127-U
Phosphatidylcholine (Egg yolk)	Avanti	840051C
Phosphatidylinositol-4,5-bisphosphate (Porcine Brain)	Avanti	840046
Sphingomyelin (Egg yolk)	Sigma	S0756
1,2-dioleoyl-sn-glycero-3-phosphocholine (DOPC)	Avanti	850375C
1,2-dioleoyl-*sn*-glycero-3-phospho-L-serine (18:1, DOPS)	Avanti	840035C
1,2-dioleoyl-sn-glycero-3-phosphoethanolamine-N-[4-(p-maleimidomethyl)cyclohexane-carboxamide] (18:1 MCC-PE)	Avanti	780201C
10 mg/mL beta casein solution	ThermoFisher	37528
10x PBS [pH 7.4]	Corning	46-013-CM
glucose oxidase from *Aspergillus niger* (225 U/mg)	Biophoretics	B01357.02
catalase	Sigma	C40-100MG Bovine Liver
Trolox	Cayman Chemicals	10011659
Dyomics 647 maleimide dye	Dyomics	647P1-03
Coenzyme A	Sigma	C3019
Sulfuric acid	Sigma	58105-2.5L-PC
C-Flat 2/2-T grids	FisherScientific	50-192-8327
Critical commercial assays		
Transcreener ADP2 FI Assay (1,000 Assay, 384 Well)	BellBrook Labs	3013-1K
Deposited data		
PDB coordinate file for p110γ-NB7 structure	PDB	8DP0
EM density file for p110γ-NB7 complex	EMD	EMD-27627
HDX-MS and phosphorylation proteomics data	PRIDE	PXD040765
Oligonucleotides		
Fwd primer for amplifying KD of PKCβII GTATTTTCAGGGCgccggtaccACGACCAACACTGTCTCCAAATTTG	Sigma	MR51F
Rvs primer for amplifying KD of PKCβII gactcgagcggccgcTTATAGCTCTTGACTTCGGGTTTTAAAAATTCAG	Sigma	MR51R
Fwd primer for amplifying N term of PKCβII CCATCACggatctggcggtagtATGGCTGACCCGGCTGCG	Sigma	MR52F
Rvs primer for amplifying N term of PKCβII GCCCTGAAAATACAGGTTTTCCTTTTCTTCCGGGACCTTGGTTCCC	Sigma	MR52R
Fwd primer for adding stop codon to PKCβII AGTCAAGAGCTAAgcggccgctcgagtctagagcctgc	Sigma	MR56F
Rvs primer for adding stop codon to PKCβII gactcgagcggccgcTTAGCTCTTGACTTCGGGTTTTAAAAATTCAG	Sigma	MR56R
Recombinant DNA		
pMultiBac-Gβ1/Gγ2	PMID:34452907	pOP737

pACEBac1-hsp110γ	PMID:34452907	MR30
pMultiBac-hsp110γ-ssp101	PMID:34452907	MR22
pMultiBac-hsp110γ-mmp84	PMID:34452907	MR24
pFastBac HRas G12V	PMID:34452907	BS9
biGBac hsp110γ/ybbr-hsp84	PMID:36842083	HP28
biGBac hsp110γ/ybbr-hsp101	PMID:36842083	HP29
his6-GST-PrescissionProtease-SNAP-RBD(K65E)	PMID:34452907	pSH936
his6TEV-HRas(1-184aa) C118S, C181S	PMID:34452907	pSH414
his6-Gγ2, SNAP-Gβ1 (DUAL FastBac)	PMID:34452907	pSH651
pACEBAC-PKCβII (internal tev cleavage site)	This paper	pMR56
pFASTBac p110α	PMID: 28515318	pOV1181
pFASTBac p110β	PMID: 28515318	pOV1182
pFASTBac p110δ	PMID: 28515318	pOV1183
pFASTBac p85β	This paper	EX21
Software and algorithms		
COOT-0.9.4.1	CCP4	https://www2.mrc-lmb.cam.ac.uk/personal/pemsley/coot/
Phenix-1.19.1	Open source	https://www.phenix-online.org/
PDBePISA (Proteins, Interfaces, Structures and Assemblies)	EMBL-EBI	https://www.ebi.ac.uk/pdbe/pisa/pistart.html
ESPript 3.0	Robert et al NAR 2014	https://espript.ibcp.fr
HDExaminer	Sierra Analytics	http://massspec.com/hdexaminer
GraphPad Prism 7	GraphPad	https://www.graphpad.com
PyMOL	Schroedinger	http://pymol.org
Compass Data Analysis	Bruker	https://www.bruker.com
ChimeraX	UCSF	https://www.rbvi.ucsf.edu/chimerax/
ImageJ/Fiji	ImageJ	https://imagej.net/software/fiji/
Nikon NIS elements	Nikon	https://www.microscope.healthcare.nikon.com/products/software/nis-elements
cryoSPARC v.3.3.2	Structura Biotechnology	https://cryosparc.com/
Other		
Sf9 insect cells for expression	Expression Systems	94-001S
Insect cell media	Expression Systems	96-001-01
Hellmanex III cleaning solution	Fisher	14-385-864
6-well sticky-side chamber	IBIDI	80608

368

369

370 *Plasmid Generation*

371 Plasmids encoding Homo sapiens p110γ (human), Mus musculus p84 (mouse), Sus
372 scrofa p101 (porcine), and Gβγ were used as previously described (Rathinaswamy et al.,
373 2023, 2021a). The class IA plasmids were also used as previously described (Dornan et
374 al., 2017; Siempelkamp et al., 2017). The pDONR223-PRKCB2 (PKCβII, uniprot
375 identifier: P05771-2) was a gift from William Hahn & David Root (Addgene plasmid
376 #23746; http://n2t.net/addgene: 23746; RRID:Addgene_23746) (Johannessen et al.,
377 2010). The PKCβII construct contains an internal TEV site that cleaves the catalytic
378 domains from the C1/C2 regulatory domains (TEV site inserted between residues 320
379 and 321 of PRKCB, uniprot identifier: P05771-2) and it was subcloned into a pACEBAC
380 Sf9 expression vector for protein purification. For purification, a 10× histidine tag, a 2×
381 strep tag, and a tobacco etch virus protease cleavage site were cloned to the N terminus
382 of the regulatory subunits for the complex and to p110γ and PKCβII for constructs without
383 regulatory subunits. Full details of the plasmids are included in the resource table.

384

385 *Virus Generation and Amplification:*

386 The plasmids encoding genes for insect cell expression were transformed into
387 DH10MultiBac cells (MultiBac, Geneva Biotech) to generate baculovirus plasmid
388 (bacmid) containing the genes of interest. Successful generation was identified by blue-
389 white colony screening and the bacmid was purified using a standard isopropanol-ethanol
390 extraction method. Bacteria were grown overnight (16 hours) in 3-5 mL 2xYT (BioBasic
391 #SD7019). Cells were spun down and the pellet was resuspended in 300 µL of 50 mM
392 Tris-HCl, pH 8.0, 10 mM EDTA, 100 mg/mL RNase A. The pellet was lysed by the addition
393 of 300 µL of 1% sodium dodecyl sulfate (SDS) (W/V), 200 mM NaOH, and the reaction
394 was neutralized by addition of 400 µL of 3.0 M potassium acetate, pH 5.5. Following
395 centrifugation at 21130 RCF and 4 °C (Rotor #5424 R), the supernatant was mixed with
396 800 µL isopropanol to precipitate bacmid DNA. Following centrifugation, the pelleted
397 bacmid DNA was washed with 500 µL 70% Ethanol three times. The pellet was then air
398 dried for 1 minute and re-suspended in 50 µL Buffer EB (10 mM Tris-Cl, pH 8.5; All buffers

399 from QIAprep Spin Miniprep Kit, Qiagen #27104). Purified bacmid was then transfected
400 into Sf9 cells. 2 mL of Sf9 cells at 0.6X106 cells/mL were aliquoted into a 6-well plate and
401 allowed to attach to form a confluent layer. Transfection reactions were prepared mixing
402 8-12 µg of bacmid DNA in 100 µL 1xPBS and 12 µg polyethyleneimine
403 (Polyethyleneimine "Max" MW 40.000, Polysciences #24765, USA) in 100 µL 1xPBS and
404 the reaction was allowed to proceed for 20-30 minutes before addition to an Sf9
405 monolayer containing well. Transfections were allowed to proceed for 5-6 days before
406 harvesting virus containing supernatant as a P1 viral stock.
407 Viral stocks were further amplified by adding P1 to Sf9 cells at ~$2x10^6$ cells/mL
408 (2/100 volume ratio). This amplification was allowed to proceed for 4-5 days and resulted
409 in a P2 stage viral stock that was used in final protein expression. Harvesting of P2 viral
410 stocks was carried out by centrifuging cell suspensions in 50 mL Falcon tubes at 2281
411 RCF (Beckman GS-15). To the supernatant containing virus, 5-10% inactivated fetal
412 bovine serum (FBS; VWR Canada #97068-085) was added and the stock was stored at
413 4°C.
414
415 *Expression and purification of PI3Kγ, PI3Kα/β/δ and PKCβ constructs:*
416 PI3Kγ *and PKCβ* constructs were expressed in Sf9 insect cells using the baculovirus
417 expression system. Following 55 hours of expression, cells were harvested by
418 centrifuging at 1680 RCF (Eppendorf Centrifuge 5810 R) and the pellets were snap-
419 frozen in liquid nitrogen. The complex was purified through a combination of nickel affinity,
420 streptavidin affinity and size exclusion chromatographic techniques.
421 Frozen insect cell pellets were resuspended in lysis buffer (20 mM Tris pH 8.0, 100
422 mM NaCl, 10 mM imidazole pH 8.0, 5% glycerol (v/v), 2 mM βME), protease inhibitor
423 (Protease Inhibitor Cocktail Set III, Sigma)) and sonicated for 2 minutes (15s on, 15s off,
424 level 4.0, Misonix sonicator 3000). Triton-X was added to the lysate to a final
425 concentration of 0.1% and clarified by spinning at 15,000 RCF at 4°C for 45 minutes
426 (Beckman Coulter JA-20 rotor). The supernatant was loaded onto a 5 mL HisTrap™ FF
427 crude column (GE Healthcare) equilibrated in NiNTA A buffer (20 mM Tris pH 8.0, 100
428 mM NaCl, 20 mM imidazole pH 8.0, 5% (v/v) glycerol, 2 mM βME). The column was

429 washed with high salt NiNTA A buffer (20 mM Tris pH 8.0, 1 M NaCl, 20 mM imidazole
430 pH 8.0, 5% (v/v) glycerol, 2 mM βME), NiNTA A buffer, 6% NiNTA B buffer (20 mM Tris
431 pH 8.0, 100 mM NaCl, 250 mM imidazole pH 8.0, 5% (v/v) glycerol, 2 mM βME) and the
432 protein was eluted with 100% NiNTA B. The eluent was loaded onto a 5 mL StrepTrap™
433 HP column (GE Healthcare) equilibrated in gel filtration buffer (20mM Tris pH 8.5, 100
434 mM NaCl, 50 mM Ammonium Sulfate and 0.5 mM TCEP). To purify *PI3Kα/β/δ*, the
435 purification protocol was performed as described above but instead the protein was eluted
436 in PI3Ka gel filtration buffer (20mM HEPES 7.5, 150mM NaCl, 0.5mM TCEP). The column
437 was washed with the corresponding gel filtration buffer and loaded with tobacco etch virus
438 protease. After cleavage on the column overnight, the PI3Kγ protein constructs were
439 eluted in gel filtration buffer. The protein was concentrated in a 50,000 MWCO Amicon
440 Concentrator (Millipore) to <1 mL and injected onto a Superdex™ 200 10/300 GL
441 Increase size-exclusion column (GE Healthcare) equilibrated in gel filtration buffer. After
442 size exclusion, the protein was concentrated, aliquoted, frozen, and stored at -80ºC. For
443 PKCβ, the protein was eluted from the strep column in gel filtration buffer, and the eluate
444 was then loaded on a 1ml HisTrap™ FF column to remove the his tagged LipTev. The
445 flowthrough was collected, and the column was washed with 2ml of gel filtration buffer.
446 These fractions were pooled and concentrated and stored at -80ºC.
447 To purify phosphorylated p110γ, the purification protocol as described above was
448 performed but PKCβ was added to the strep column at a molar ratio of 1:3 (PKCβII:p110)
449 along with LipTEV, 20 mM $MgCl_2$ and 1mM ATP and allowed to incubate on ice for 4
450 hours. The protein was eluted by adding 7 ml of gel filtration buffer and treated with a
451 second dose of PKCβ (same ratio as above) and allowed to incubate on ice for another
452 3 hours. For non-phosphorylated p110, same protocol was followed with the exception in
453 the addition of PKCβ. Both the proteins were concentrated in a 50,000 MWCO Amicon
454 Concentrator (Millipore) to <1 mL and injected onto a Superdex™ 200 10/300 GL
455 Increase size-exclusion column (GE Healthcare) equilibrated in gel filtration buffer. The
456 final phosphorylation level of the two sites was characterised by mass spectrometry, with
457 these values being 92% and 90.8%, for S582 and S594/S595 respectively. After size
458 exclusion, the protein was concentrated, aliquoted, frozen, and stored at -80ºC.

459

460 *Expression and Purification of lipidated Gβγ for kinase activity assays:*

461 Full length, lipidated human *Gβγ* (Gβ1γ2) was expressed in Sf9 insect cells and
462 purified as described previously. After 65 hours of expression, cells were harvested, and
463 the pellets were frozen as described above. Pellets were resuspended in lysis buffer (20
464 mM HEPES pH 7.7, 100 mM NaCl, 10 mM βME, protease inhibitor (Protease Inhibitor
465 Cocktail Set III, Sigma)) and sonicated for 2 minutes (15s on, 15s off, level 4.0, Misonix
466 sonicator 3000). The lysate was spun at 500 RCF (Eppendorf Centrifuge 5810 R) to
467 remove intact cells and the supernatant was centrifuged again at 25,000 RCF for 1 hour
468 (Beckman Coulter JA-20 rotor). The pellet was resuspended in lysis buffer and sodium
469 cholate was added to a final concentration of 1% and stirred at 4°C for 1 hour. The
470 membrane extract was clarified by spinning at 10,000 RCF for 30 minutes (Beckman
471 Coulter JA-20 rotor). The supernatant was diluted 3 times with NiNTA A buffer (20 mM
472 HEPES pH 7.7, 100 mM NaCl, 10 mM Imidazole, 0.1% C12E10, 10mM βME) and loaded
473 onto a 5 mL HisTrap™ FF crude column (GE Healthcare) equilibrated in the same buffer.
474 The column was washed with NiNTA A, 6% NiNTA B buffer (20 mM HEPES pH 7.7, 25
475 mM NaCl, 250 mM imidazole pH 8.0, 0.1% C12E10, 10 mM βME) and the protein was
476 eluted with 100% NiNTA B. The eluent was loaded onto HiTrap™ Q HP anion exchange
477 column equilibrated in Hep A buffer (20 mM Tris pH 8.0, 8 mM CHAPS, 2 mM
478 Dithiothreitol (DTT)). A gradient was started with Hep B buffer (20 mM Tris pH 8.0, 500
479 mM NaCl, 8 mM CHAPS, 2 mM DTT) and the protein was eluted in ~50% Hep B buffer.
480 The eluent was concentrated in a 30,000 MWCO Amicon Concentrator (Millipore) to < 1
481 mL and injected onto a Superdex™ 75 10/300 GL size exclusion column (GE Healthcare)
482 equilibrated in Gel Filtration buffer (20 mM HEPES pH 7.7, 100 mM NaCl, 10 mM CHAPS,
483 2 mM TCEP). Fractions containing protein were pooled, concentrated, aliquoted, frozen
484 and stored at -80 °C.

485

486 *Expression and purification of nanobody:*

487 Nanobody NB7-PIK3CG with a C-terminal 6X His tag was expressed from a
488 pMESy4 vector in the periplasm of WK6 *E.coli*. A 1L culture was grown to OD600 of 0.7

489 in Terrific Broth containing 0.1% glucose and 2mM MgCl2 in the presence of 100 µg/mL
490 ampicillin and was induced with 0.5 mM isopropyl-β-D-thiogalactoside (IPTG). Cells were
491 harvested the following day by centrifuging at 2500 RCF (Eppendorf Centrifuge 5810 R)
492 and the pellet was snap-frozen in liquid nitrogen. The frozen pellet was resuspended in
493 15 mL of TES buffer containing 200 mM Tris pH 8.0, 0.5mM ethylenediaminetetraacetic
494 acid (EDTA) and 500 mM Sucrose and was mixed for 45 minutes at 4°C. To this mixture,
495 30 mL of TES buffer diluted four times in water was added and mixed for 45 minutes at
496 4°C to induce osmotic shock. The lysate was clarified by centrifuging at 14,000 rpm for
497 15 minutes (Beckman Coulter JA-20 rotor). Imidazole was added to the supernatant to
498 final concentration of 10mM loaded onto a 5 mL HisTrap™ FF crude column (GE
499 Healthcare) equilibrated in NiNTA A buffer (20 mM Tris pH 8.0, 100 mM NaCl, 20 mM
500 imidazole pH 8.0, 5% (v/v) glycerol, 2 mM β-mercaptoethanol (βME)). The column was
501 washed with high salt NiNTA A buffer (20 mM Tris pH 8.0, 1 M NaCl, 20 mM imidazole
502 pH 8.0, 5% (v/v) glycerol, 2 mM βME), followed by 100% NiNTA A buffer, then a 6%
503 NiNTA B wash buffer (20 mM Tris pH 8.0, 100 mM NaCl, 250 mM imidazole pH 8.0, 5%
504 (v/v) glycerol, 2 mM βME) and the protein was eluted with 100% NiNTA B. The eluent
505 was concentrated in a 10,000 MWCO Amicon Concentrator (Millipore) to <1 mL and
506 injected onto a Superdex™ 75 10/300 GL Increase size-exclusion column (GE
507 Healthcare) equilibrated in gel filtration buffer (20mM Tris pH 8.5, 100 mM NaCl, 50 mM
508 Ammonium Sulfate and 0.5 mM tris(2-carboxyethyl) phosphine (TCEP)). Following size
509 exclusion, the protein was concentrated, frozen and stored at -80°C.
510
511 *Phosphorylation analysis*
512 For the dose–response phosphorylation of p110γ, p110/p84, and p110/p101, each
513 protein or complex (750nM) was mixed with ATP (200 μM), GFB (20mM Tris pH 8.5, 100
514 mM NaCl, 50 mM Ammonium Sulfate and 0.5 mM TCEP), $MgCl_2$(20mM) and various
515 amounts of PKC (4 µg, 800 ng, 160 ng, 32 ng, 6.4 ng, and 0 ng). Reactions were
516 incubated for three hours on ice and quenched with 50 μL of ice-cold acidic quench buffer
517 (0.7 M guanidine-HCl, 1% formic acid). followed by immediate freezing using liquid
518 nitrogen and storage at –80 °C.

519 For the experiment studying the effect of nanobody on phosphorylation, p110γ or
520 p110/p101, (500nM) was mixed with ATP (1 mM), GFB (20mM Tris pH 8.5, 100 mM NaCl,
521 50 mM Ammonium Sulfate and 0.5 mM TCEP), $MgCl_2$(20mM), with nanobody and PKC
522 present at 1200 nM and 500nM, respectively. Reactions were incubated for one hour at
523 room temperature and quenched with 54 μL of ice-cold acidic quench buffer (0.7 M
524 guanidine-HCl, 1% formic acid) followed by immediate freezing using liquid nitrogen and
525 storage at –80 °C.
526 Phosphorylation of all proteins was confirmed using Mass spectrometry and
527 PEAKS7 analysis. The phosphorylated and non-phosphorylated peptide ratios were
528 determined by generating extracted ion chromatograms for each peptide using their
529 molecular formula and charge state in the Bruker Compass Data Analysis software. The
530 area under each extracted curve was then extracted. The full MS quantification of each
531 of the phosphorylated and non-phosphorylated peptide is provided in the source data.
532
533
534 *Lipid vesicle preparation for kinase activity assays*
535 Lipid vesicles containing 5% brain phosphatidylinositol 4,5- bisphosphate (PIP2), and
536 95% brain phosphatidylserine (PS), were prepared by mixing the lipids solutions in
537 organic solvent. The solvent was evaporated in a stream of argon following which the lipid
538 film was desiccated in a vacuum for 45 minutes. The lipids were resuspended in lipid
539 buffer (20 mM HEPES pH 7.0, 100 mM NaCl and 10 % glycerol) and the solution was
540 vortexed for 5 minutes followed by sonication for 15 minutes. The vesicles were then
541 subjected to ten freeze thaw cycles and extruded 11 times through a 100-nm filter (T&T
542 Scientific: TT-002-0010). The extruded vesicles were sub-aliquoted and stored at -80°C.
543 Final vesicle concentration was 2 mg/mL.
544
545 *Kinase Assays*
546 All kinase assays were done using Transcreener ADP2 Fluorescence Intensity (FI)
547 assays (Bellbrook labs) which measures ADP production. All assays used super-lipid
548 vesicles [5% phosphatidylinositol 4,5-bisphosphate (PI(4,5)P2), and 95%

549 phosphatidylserine (PS)] at final concentration of 0.5 mg/mL, and ATP at a final
550 concentration of 100 μM.
551 For assays measuring the inhibition by nanobody, 4X kinase (final concentration:
552 330 nM for p110γ, 300nM for p110γ/p84 and 12nM for p110γ/p101) was mixed with
553 varying 4X concentrations of nanobody (final concentration: 2μM – 2.7nM) or kinase
554 buffer (20mM HEPES pH 7.5, 100mM NaCl, 3mM $MgCl_2$, 0.03% CHAPS, 2mM TCEP,
555 and 1mM EGTA) and allowed to sit on ice for 15 minutes. 2 μl of protein mix was mixed
556 with 2 μl of lipid solution containing Gβγ (1μM final concentration), ATP (100 μM), Super
557 lipid (0.5mg/ml final concentration), and lipid buffer (25mM HEPES pH 7, 5% Glycerol,
558 and 100mM NaCl) and incubated at room temperature for 60 minutes.
559 For assays comparing the difference in activation between phosphorylated and non-
560 phosphorylated p110γ, 2X kinase (final concentrations: 1μM – 12.3nM) was mixed with
561 2X lipid solutions containing ATP (100 μM), and lipid buffer and either nanobody (3 μM
562 final concentration), Super lipid (0.5mg/ml final concentration) or both nanobody and lipid.
563 The reaction was incubated at room temperature for 60 minutes.
564 After the 60-minute incubation, all reactions were stopped with 4 μL of 2X stop and
565 detect solution containing Stop and Detect buffer (20mM HEPES,0.02% Brij-35, 400mM
566 40mM EDTA pH 7.5), 8 nM ADP Alexa Fluor 594 Tracer and 93.7 μg/mL ADP2 Antibody
567 IRDye QC-1, covered and incubated at room temperature for 1 hr before reading the
568 fluorescence. The fluorescence intensity was measured using a SpectraMax M5 plate
569 reader at excitation 590 nm and emission 620 nm. All data was normalized against the
570 appropriate measurements obtained for 100 μM ATP and 100 μM ADP with no kinase.
571 The percent ATP turnover was interpolated using a standard curve (0.1-100 μM ADP).
572 Interpolated values were then used to calculate the specific activity of the enzyme.
573
574 *Biolayer interferometry*
575 All Biolayer interferometry experiments were performed using the Octet K2 (Fortebio Inc.).
576 When comparing nanobody binding to each complex, His-tagged nanobody was
577 immobilized on an Anti-Penta-His biosensor for 600s, and the sensor was dipped into
578 solutions of varying concentrations of p110γ, p110p84, and p110p101 (50 nM – 1.9 nM)

579 for 600s followed by a 1200s dissociation step in Octet Buffer (20 mM tris pH 8.5, 100
580 mM NaCl, 50 mM ammonium sulfate, 0.1% bovine serum albumin, and 0.02% Tween
581 20). Experiments comparing class IA PI3K versus class IB PI3K used 500 nM nanobody
582 loaded on the Octet tip, and 50 nM of PI3Ks. When comparing nanobody binding to
583 phosphorylated and unphosphorylated p110γ, His-tagged nanobody was immobilized on
584 an Anti-Penta-His biosensor for 600 s, and the sensor was dipped into solutions of either
585 phosphorylated or non-phosphorylated p110γ at a final concentration of 25 nM for 600s
586 followed by a dissociation step for 600s. The average K_D (dissociation constant) was
587 calculated from the binding curves based on their global fit to a 1:1 binding model.
588
589 *Supported lipid bilayer TIRF microscopy experiments*
590 The membrane binding dynamics of Dy647-p84-p110γ were measured in the
591 absence and presence of nanobody 7 (NB7) using TIRF microscopy. As previously
592 described (Rathinaswamy et al., 2023), supported lipid bilayers were formed using 50 nm
593 extruded small unilamellar vesicles (SUVs) containing the following lipids: 1,2-dioleoyl-
594 sn-glycero-3-phosphocholine (18:1 DOPC, Avanti # 850375C), 1,2-dioleoyl-*sn*-glycero-3-
595 phospho-L-serine (18:1 DOPS, Avanti # 840035C), 1,2-dioleoyl-sn-glycero-3-
596 phosphoethanolamine-N-[4-(p-maleimidomethyl)cyclohexane-carboxamide] (18:1 MCC-
597 PE, Avanti # 780201C). Lipid compositions reported in figure legends represent the molar
598 percentage of each lipid species.
599 To create SLBs, a total concentration of 0.25 mM lipids was solvated in 1x PBS
600 [pH 7.4] and deposited on Piranha etched glass coverslips (25 x 75 mm) adhered to an
601 IBIDI chamber. After a 30-minute incubation, membranes were washed with 4 mL of 1x
602 PBS [pH 7.4] and then blocked for 10 minutes with 1 mg/mL beta casein (Thermo
603 FisherSci, Cat# 37528) in 1x PBS [pH 7.4] (Corning, Cat# 46-013-CM). To conjugate H-
604 Ras to maleimide lipids (MCC-PE), blocked membranes were incubated with 30 μM H-
605 Ras(GDP) in buffer containing 1x PBS [pH 7.4], 1 mM $MgCl_2$, 50 μM GDP, and 0.1 mM
606 TCEP for 2 hours. The membrane conjugation reaction was terminated after 2 hours with
607 1x PBS [pH 7.4] containing 5 mM β-mercaptoethanol (βME). Membranes were then

608 washed and stored in 1x PBS [pH 7.4] until performing the TIRF-M membrane binding
609 experiments. H-Ras was purified as previously described (Rathinaswamy et al., 2023).
610 To perform the TIRF-M membrane binding assays, 200 nM farnesyl-$G\beta\gamma$ was
611 equilibrated into the supported membranes for 30 minutes. In parallel, nucleotide
612 exchange of H-Ras(GDP) was performed by adding 50 nM guanine nucleotide exchange
613 factor (SosCat) in 1x PBS [pH 7.4], 1 mM $MgCl_2$, 50 μM GDP. To measure membrane
614 binding, Dy647-p84-p110γ was diluted into the following buffer: 20 mM HEPES [pH 7.0],
615 150 mM NaCl, 50 μM GTP, 1 mM ATP, 5 mM $MgCl_2$, 0.5 mM EGTA, 20 mM glucose, 200
616 μg/mL beta casein (ThermoScientific, Cat# 37528), 20 mM BME, 320 μg/mL glucose
617 oxidase (Serva, #22780.01 *Aspergillus niger*), 50 μg/mL catalase (Sigma, #C40-100MG
618 Bovine Liver), and 2 mM Trolox. Trolox was prepared as previously described (Hansen
619 et al., 2019). Perishable reagents (i.e. glucose oxidase, catalase, and Trolox) were added
620 10 minutes before image acquisition.
621 TIRF-M experiments were performed using an inverted Nikon Ti2 microscope with
622 a 100x Nikon (1.49 NA) oil immersion objective. The x-axis and y-axis positions were
623 controlled using a Nikon motorized stage. Dy647-p84-p110γ was excited with a 637 nm
624 diode laser (OBIS laser diode, Coherent Inc. Santa Clara, CA) controlled with an acousto-
625 optic tunable filter (AOTF) and laser launch built by Vortran (Sacramento, CA). The power
626 output measured through the objective for single particle imaging was 1-3 mW. Excitation
627 light passing through quad multi-pass dichroic filter cube (Semrock). Fluorescence
628 emission passed through Nikon emission filter wheel containing the following 25 mm
629 ET700/75M emission filters (Semrock) before being detected on iXion Life 897 EMCCD
630 camera (Andor Technology Ltd., UK). All TIRF-M experiments were performed at room
631 temperature (23°C). Microscope hardware was controlled using Nikon NIS elements.
632 Data analysis was performed using ImageJ/Fiji and Prism graphing program.
633
634 *Cryo-EM Sample Preparation and Data Collection*
635 3 μL of purified nanobody-bound p110γ at 0.45 mg/ml was adsorbed onto C-Flat 2/2-T
636 grids that were glow discharged for 25 s at 15 mA. Grids were then plunged into liquid
637 ethane using a Vitrobot Mark IV (Thermo Fisher Scientific) with the following settings: -5

638 blot force, 1.5 s blot time, 100% humidity and 4 °C. Vitrified specimens were screened for
639 ice and particle quality at the UBC High resolution macromolecular electron microscopy
640 (HRMEM) facility using a 200-kV Glacios transmission electron microscope equipped with
641 a Falcon 3EC direct electron detector (DED). Clipped grids were sent to the Pacific
642 Northwest Cryo-EM Center (PNCC) where 7,322 movies were collected using a Titan
643 Krios equipped with a Gatan K3 DED and a BioQuantum K3 energy filter with a slit width
644 of 20 eV. The movies were collected at a physical pixel size of 0.830 Å/pix and a total
645 dose of $50e^{-}/Å^{2}$ over 50 frames.

646

647 *Cryo-EM image analysis*

648 The data were processed using cryoSPARC v.3.3.2 (Punjani et al., 2017). The
649 movies were pre-processed by patch motion correction using default settings except
650 Fourier-cropping by a factor of 2, followed by patch CTF estimation using default settings.
651 A 3D map of PI3K p110γ-p101 complex (EMD-23808) was used to create 2D projections
652 for use as templates to auto-pick 1,463,553 particles. Particles were extracted with a box
653 size of 380 pixels, Fourier cropped to a box size of 96 pixels and subjected to 2D
654 classification. After discarding classes with obvious noise and no features, 795,162
655 particles were used for multiple rounds of *ab initio* reconstruction and heterogeneous
656 refinement using 4 or 5 classes. 365,178 particles, which generated the two best 3D
657 reconstruction, were used to carry out Per-particle local-motion correction with 760 pixels
658 box size later downsized to 380 pixels followed by several rounds of *ab initio*
659 reconstruction and heterogeneous refinement using 3 or 5 classes. 149,603 from best
660 class were further refined by homogeneous refinement and a final Non-Uniform (NU)-
661 refinement which generated a reconstruction with an overall resolution of 3.02 Å based
662 on the Fourier shell correlation (FSC) 0.143 criterion.

663

664 *Building the structural model of p110γ-NB7*

665 The previous structural model of full length p110γ from the complex of p110γ-
666 p101(PDB: 7MEZ) (Rathinaswamy et al., 2021a) was fit into the map using Chimera

667 (Pettersen et al., 2004). A model of the nanobody was generated using Alphafold2 using
668 the Colabfold v1.5.2 server (Mirdita et al., 2022). The CDR loops were removed from this
669 initial model, and the remaining nanobody was fit into the map using Chimera. The final
670 structure was built by iterative rounds of automated model building in Phenix, manual
671 model building in COOT (Emsley et al., 2010), and refinement in
672 Phenix.real_space_refine using realspace, rigid body, and adp refinement with tight
673 secondary structure restraints (Afonine et al., 2012). This allowed for unambiguous
674 building of the CDRs of the nanobody, and their interface with p110γ. The full refinement
675 and validation statistics are shown in Supplemental table 1.
676
677 *Hydrogen Deuterium eXchange Mass Spectrometry*
678 Exchange reactions to assess differences in p110γ upon phosphorylation were
679 carried out at 20°C in 10 μL volumes with final concentrations of 1.6 μM for both apo and
680 phosphorylated p110γ. A total of two conditions were assessed: p110γ apo and PKCβ
681 phosphorylated p110γ. The hydrogen-deuterium exchange reaction was initiated by the
682 addition of 8 μL D_2O buffer (94.3% D_2O, 100 mM NaCl, 20 mM HEPES pH 7.5) to the 2
683 μL protein for a final D_2O concentration of 75.4%. Exchange was carried out over five
684 time points (3s on ice, and 3s, 30s, 300s and 3000s at 20°C) and the reaction was
685 quenched with addition of 60 μL of ice-cold acidic quench buffer (0.7 M guanidine-HCl,
686 1% formic acid). After quenching, samples were immediately frozen in liquid nitrogen and
687 stored at -80°C. All reactions were carried out in triplicate.
688
689 *Protein Digestion and MS/MS Data Collection*: Protein samples were rapidly
690 thawed and injected onto an integrated fluidics system containing a HDx-3 PAL liquid
691 handling robot and climate-controlled chromatography system (LEAP Technologies), a
692 Dionex Ultimate 3000 UHPLC system, as well as an Impact HD QTOF Mass spectrometer
693 (Bruker). The protein was run over two immobilized pepsin columns (Applied Biosystems;
694 Poroszyme™ Immobilized Pepsin Cartridge, 2.1 mm x 30 mm; Thermo-Fisher 2-3131-
695 00; at 10°C and 2°C respectively) at 200 µL/min for 3 minutes. The resulting peptides
696 were collected and desalted on a C18 trap column [Acquity UPLC BEH C18 1.7 mm

697 column (2.1 x 5 mm); Waters 186003975]. The trap was subsequently eluted in line with
698 an ACQUITY 1.7 μm particle, 100 x 1 mm2 C18 UPLC column (Waters 186002352), using
699 a gradient of 3-35% B (buffer A, 0.1% formic acid; buffer B, 100% acetonitrile) over 11
700 min immediately followed by a gradient of 35-80% B over 5 minutes. MS experiments
701 acquired over a mass range from 150 to 2200 mass/charge ratio (m/z) using an
702 electrospray ionization source operated at a temperature of 200°C and a spray voltage of
703 4.5 kV.
704
705 *Peptide Identification*: Peptides were identified using data-dependent acquisition
706 following tandem MS/MS experiments (0.5 s precursor scan from 150-2000 m/z; twelve
707 0.25 s fragment scans from 150-2000 m/z). MS/MS datasets were analyzed using
708 PEAKS7 (PEAKS), and a false discovery rate was set at 0.1% using a database of purified
709 proteins and known contaminants. Same approach was used to identify phosphorylated
710 and non-phosphorylated peptides for our in-vitro phosphorylation experiments, with
711 variable phosphorylation of STY residues was added to the search. The search
712 parameters were set with a precursor tolerance of 20 parts per million, fragment mass
713 error 0.02 Da, and charge states from 1 to 8, with a selection criterion of peptides that
714 had a −10logP score of >24.03 for phosphorylated and >23.05 for non-phosphorylated.
715 The MS/MS spectra of the PKC phosphorylated peptides are included in Fig S3.
716
717 *Mass Analysis of Peptide Centroids and Measurement of Deuterium Incorporation:*
718 HD-Examiner Software (Sierra Analytics) was used to automatically calculate the level of
719 deuterium incorporation into each peptide. All peptides were manually inspected for
720 correct charge state, correct retention time, and appropriate selection of isotopic
721 distribution. Deuteration levels were calculated using the centroid of the experimental
722 isotope clusters. HDX-MS results are presented with no correction for back exchange
723 shown in the Source data, with the only correction being applied correcting for the
724 deuterium oxide percentage of the buffer used in the exchange (75.4%). Changes in any
725 peptide at any time point greater than specified cut-offs (5% and 0.45 Da) and with an
726 unpaired, two-tailed t-test value of $p<0.01$ was considered significant. A number of

727 peptides in the helical domain showed isotope distributions consistent with EX1 H/D
728 exchange. Attempts to define the relative percentages of each population using
729 HDExaminer were extremely noisy, so representative EX1 profiles are shown in Fig. 3C.
730 The raw peptide deuterium incorporation graphs for a selection of peptides with significant
731 differences are shown in Fig. 4D, with the raw data for all analysed peptides in the source
732 data. To allow for visualization of differences across all peptides, we utilized number of
733 deuteron difference (#D) plots (Fig. 4B). These plots show the total difference in
734 deuterium incorporation over the entire H/D exchange time course, with each point
735 indicating a single peptide. The data analysis statistics for all HDX-MS experiments are
736 in Supplemental Table 2 according to the guidelines of (Masson et al., 2019). The mass
737 spectrometry proteomics data have been deposited to the ProteomeXchange Consortium
738 via the PRIDE partner repository (Perez-Riverol et al., 2022) with the dataset identifier
739 PXD040765.
740

741 **References**

742 Afonine PV, Grosse-Kunstleve RW, Echols N, Headd JJ, Moriarty NW, Mustyakimov M,
743 Terwilliger TC, Urzhumtsev A, Zwart PH, Adams PD. 2012. Towards automated
744 crystallographic structure refinement with phenix.refine. *Acta Crystallogr D Biol*
745 *Crystallogr* **68**:352–367. doi:10.1107/S0907444912001308
746 Angulo I, Vadas O, Garçon F, Banham-Hall E, Plagnol V, Leahy TR, Baxendale H,
747 Coulter T, Curtis J, Wu C, Blake-Palmer K, Perisic O, Smyth D, Maes M, Fiddler
748 C, Juss J, Cilliers D, Markelj G, Chandra A, Farmer G, Kielkowska A, Clark J,
749 Kracker S, Debré M, Picard C, Pellier I, Jabado N, Morris JA, Barcenas-Morales
750 G, Fischer A, Stephens L, Hawkins P, Barrett JC, Abinun M, Clatworthy M,
751 Durandy A, Doffinger R, Chilvers ER, Cant AJ, Kumararatne D, Okkenhaug K,
752 Williams RL, Condliffe A, Nejentsev S. 2013. Phosphoinositide 3-kinase δ gene
753 mutation predisposes to respiratory infection and airway damage. *Science*
754 **342**:866–871. doi:10.1126/science.1243292
755 Becattini B, Marone R, Zani F, Arsenijevic D, Seydoux J, Montani J, Dulloo A, Thorens
756 B, Preitner F, Wymann M, Solinas G. 2011. PI3Kgamma within a
757 nonhematopoietic cell type negatively regulates diet-induced thermogenesis and
758 promotes obesity and insulin resistance. *Proc Natl Acad Sci USA* **108**:E854-63.
759 doi:10.1073/pnas.1106698108/-/DCSupplemental
760 Bell K, Sunose M, Ellard K, Cansfield A, Taylor J, Miller W, Ramsden N, Bergamini G,
761 Neubauer G. 2012. SAR studies around a series of triazolopyridines as potent
762 and selective PI3Kγ inhibitors. *Bioorg Med Chem Lett* **22**:5257–5263.
763 doi:10.1016/j.bmcl.2012.06.049

764 Bohnacker T, Marone R, Collmann E, Calvez R, Hirsch E, Wymann M. 2009.
765 PI3Kgamma adaptor subunits define coupling to degranulation and cell motility
766 by distinct PtdIns(3,4,5)P3 pools in mast cells. *Sci Signal* **2**:ra27.
767 doi:10.1126/scisignal.2000259
768 Bohnacker T, Prota AE, Beaufils F, Burke JE, Melone A, Inglis AJ, Rageot D, Sele AM,
769 Cmiljanovic V, Cmiljanovic N, Bargsten K, Aher A, Akhmanova A, Díaz JF,
770 Fabbro D, Zvelebil M, Williams RL, Steinmetz MO, Wymann MP. 2017.
771 Deconvolution of Buparlisib's mechanism of action defines specific PI3K and
772 tubulin inhibitors for therapeutic intervention. *Nat Commun* **8**:14683.
773 doi:10.1038/ncomms14683
774 Breasson L, Becattini B, Sardi C, Molinaro A, Zani F, Marone R, Botindari F,
775 Bousquenaud M, Ruegg C, Wymann MP, Solinas G. 2017. PI3Kγ activity in
776 leukocytes promotes adipose tissue inflammation and early-onset insulin
777 resistance during obesity. *Sci Signal* **10**:eaaf2969. doi:10.1126/scisignal.aaf2969
778 Burke JE. 2018. Structural Basis for Regulation of Phosphoinositide Kinases and Their
779 Involvement in Human Disease. *Mol Cell* **71**:653–673.
780 doi:10.1016/j.molcel.2018.08.005
781 Burke JE, Perisic O, Masson GR, Vadas O, Williams RL. 2012. Oncogenic mutations
782 mimic and enhance dynamic events in the natural activation of phosphoinositide
783 3-kinase p110α (PIK3CA). *Proc Natl Acad Sci USA* **109**:15259–15264.
784 doi:10.1073/pnas.1205508109
785 Burke JE, Vadas O, Berndt A, Finegan T, Perisic O, Williams RL. 2011. Dynamics of the
786 phosphoinositide 3-kinase p110δ interaction with p85α and membranes reveals
787 aspects of regulation distinct from p110α. *Structure* **19**:1127–1137.
788 doi:10.1016/j.str.2011.06.003
789 Burke JE, Williams RL. 2015. Synergy in activating class I PI3Ks. *Trends in Biochemical*
790 *Sciences* **40**:88–100. doi:10.1016/j.tibs.2014.12.003
791 Burke JE, Williams RL. 2013. Dynamic steps in receptor tyrosine kinase mediated
792 activation of class IA phosphoinositide 3-kinases (PI3K) captured by H/D
793 exchange (HDX-MS). *Adv Biol Regul* **53**:97–110. doi:10.1016/j.jbior.2012.09.005
794 Campa CC, Silva RL, Margaria JP, Pirali T, Mattos MS, Kraemer LR, Reis DC, Grosa
795 G, Copperi F, Dalmarco EM, Lima-Júnior RCP, Aprile S, Sala V, Dal Bello F,
796 Prado DS, Alves-Filho JC, Medana C, Cassali GD, Tron GC, Teixeira MM,
797 Ciraolo E, Russo RC, Hirsch E. 2018. Inhalation of the prodrug PI3K inhibitor
798 CL27c improves lung function in asthma and fibrosis. *Nat Commun* **9**:5232–16.
799 doi:10.1038/s41467-018-07698-6
800 Camps M, Rückle T, Ji H, Ardissone V, Rintelen F, Shaw J, Ferrandi C, Chabert C,
801 Gillieron C, Françon B, Martin T, Gretener D, Perrin D, Leroy D, Vitte P-A, Hirsch
802 E, Wymann MP, Cirillo R, Schwarz MK, Rommel C. 2005. Blockade of
803 PI3Kgamma suppresses joint inflammation and damage in mouse models of
804 rheumatoid arthritis. *Nat Med* **11**:936–943. doi:10.1038/nm1284
805 De Henau O, Rausch M, Winkler D, Campesato LF, Liu C, Cymerman DH, Budhu S,
806 Ghosh A, Pink M, Tchaicha J, Douglas M, Tibbitts T, Sharma S, Proctor J,
807 Kosmider N, White K, Stern H, Soglia J, Adams J, Palombella VJ, McGovern K,

808 Kutok JL, Wolchok JD, Merghoub T. 2016. Overcoming resistance to checkpoint
809 blockade therapy by targeting PI3Kγ in myeloid cells. *Nature* **539**:443–447.
810 doi:10.1038/nature20554
811 Deladeriere A, Gambardella L, Pan D, Anderson KE, Hawkins PT, Stephens LR. 2015.
812 The regulatory subunits of PI3Kγ control distinct neutrophil responses. *Sci Signal*
813 **8**:ra8. doi:10.1126/scisignal.2005564
814 Dornan GL, Siempelkamp BD, Jenkins ML, Vadas O, Lucas CL, Burke JE. 2017.
815 Conformational disruption of PI3Kδ regulation by immunodeficiency mutations in
816 PIK3CD and PIK3R1. *Proc Natl Acad Sci USA* **114**:1982–1987.
817 doi:10.1073/pnas.1617244114
818 Emsley P, Lohkamp B, Scott WG, Cowtan K. 2010. Features and development of Coot.
819 *Acta Crystallogr D Biol Crystallogr* **66**:486–501.
820 doi:10.1107/S0907444910007493
821 Evans CA, Liu T, Lescarbeau A, Nair SJ, Grenier L, Pradeilles JA, Glenadel Q, Tibbitts
822 T, Rowley AM, DiNitto JP, Brophy EE, O'Hearn EL, Ali JA, Winkler DG, Goldstein
823 SI, O'Hearn P, Martin CM, Hoyt JG, Soglia JR, Cheung C, Pink MM, Proctor JL,
824 Palombella VJ, Tremblay MR, Castro AC. 2016. Discovery of a Selective
825 Phosphoinositide-3-Kinase (PI3K)-γ Inhibitor (IPI-549) as an Immuno-Oncology
826 Clinical Candidate. *ACS Med Chem Lett* **7**:862–867.
827 doi:10.1021/acsmedchemlett.6b00238
828 Gangadhara G, Dahl G, Bohnacker T, Rae R, Gunnarsson J, Blaho S, Öster L,
829 Lindmark H, Karabelas K, Pemberton N, Tyrchan C, Mogemark M, Wymann MP,
830 Williams RL, Perry MWD, Papavoine T, Petersen J. 2019. A class of highly
831 selective inhibitors bind to an active state of PI3Kγ. *Nature Chemical Biology*
832 **15**:348–357. doi:10.1038/s41589-018-0215-0
833 Hansen SD, Huang WYC, Lee YK, Bieling P, Christensen SM, Groves JT. 2019.
834 Stochastic geometry sensing and polarization in a lipid kinase-phosphatase
835 competitive reaction. *Proc Natl Acad Sci U S A* **116**:15013–15022.
836 doi:10.1073/pnas.1901744116
837 Hawkins PT, Stephens LR. 2015. PI3K signalling in inflammation. *Biochim Biophys Acta*
838 **1851**:882–897. doi:10.1016/j.bbalip.2014.12.006
839 Jenkins ML, Ranga-Prasad H, Parson MAH, Harris NJ, Rathinaswamy MK, Burke JE.
840 2023. Oncogenic mutations of PIK3CA lead to increased membrane recruitment
841 driven by reorientation of the ABD, p85 and C-terminus. *Nat Commun* **14**:181.
842 doi:10.1038/s41467-023-35789-6
843 Jin JR, Gogvadze E, Xavier AR, Bohnacker T, Voelzmann J, Wymann MP. 2020. PI3Kγ
844 Regulatory Protein p84 Determines Mast Cell Sensitivity to Ras Inhibition-Moving
845 Towards Cell Specific PI3K Targeting? *Front Immunol* **11**:585070.
846 doi:10.3389/fimmu.2020.585070
847 Johannessen CM, Boehm JS, Kim SY, Thomas SR, Wardwell L, Johnson LA, Emery
848 CM, Stransky N, Cogdill AP, Barretina J, Caponigro G, Hieronymus H, Murray
849 RR, Salehi-Ashtiani K, Hill DE, Vidal M, Zhao JJ, Yang X, Alkan O, Kim S, Harris
850 JL, Wilson CJ, Myer VE, Finan PM, Root DE, Roberts TM, Golub T, Flaherty KT,
851 Dummer R, Weber BL, Sellers WR, Schlegel R, Wargo JA, Hahn WC, Garraway

852 LA. 2010. COT drives resistance to RAF inhibition through MAP kinase pathway
853 reactivation. *Nature* **468**:968–972. doi:10.1038/nature09627
854 Kaneda MM, Cappello P, Nguyen AV, Ralainirina N, Hardamon CR, Foubert P, Schmid
855 MC, Sun P, Mose E, Bouvet M, Lowy AM, Valasek MA, Sasik R, Novelli F, Hirsch
856 E, Varner JA. 2016a. Macrophage PI3Kγ Drives Pancreatic Ductal
857 Adenocarcinoma Progression. *Cancer Discov* **6**:870–885. doi:10.1158/2159-
858 8290.CD-15-1346
859 Kaneda MM, Messer KS, Ralainirina N, Li H, Leem CJ, Gorjestani S, Woo G, Nguyen
860 AV, Figueiredo CC, Foubert P, Schmid MC, Pink M, Winkler DG, Rausch M,
861 Palombella VJ, Kutok J, McGovern K, Frazer KA, Wu X, Karin M, Sasik R, Cohen
862 EEW, Varner JA. 2016b. PI3Kγ is a molecular switch that controls immune
863 suppression. *Nature* **539**:437–442. doi:10.1038/nature19834
864 Kurig B, Shymanets A, Bohnacker T, Prajwal, Brock C, Ahmadian MR, Schaefer M,
865 Gohla A, Harteneck C, Wymann MP, Jeanclos E, Nürnberg B. 2009. Ras is an
866 indispensable coregulator of the class IB phosphoinositide 3-kinase
867 p87/p110gamma. *Proc Natl Acad Sci USA* **106**:20312–20317.
868 doi:10.1073/pnas.0905506106
869 Laffargue M, Calvez R, Finan P, Trifilieff A, Barbier M, Altruda F, Hirsch E, Wymann
870 MP. 2002. Phosphoinositide 3-kinase gamma is an essential amplifier of mast
871 cell function. *Immunity* **16**:441–451.
872 Lanahan SM, Wymann MP, Lucas CL. 2022. The role of PI3Kγ in the immune system:
873 new insights and translational implications. *Nat Rev Immunol*.
874 doi:10.1038/s41577-022-00701-8
875 Lawrence MS, Stojanov P, Mermel CH, Robinson JT, Garraway LA, Golub TR,
876 Meyerson M, Gabriel SB, Lander ES, Getz G. 2014. Discovery and saturation
877 analysis of cancer genes across 21 tumour types. *Nature* **505**:495–501.
878 doi:10.1038/nature12912
879 Li H, Prever L, Hirsch E, Gulluni F. 2021. Targeting PI3K/AKT/mTOR Signaling Pathway
880 in Breast Cancer. *Cancers (Basel)* **13**:3517. doi:10.3390/cancers13143517
881 Li Z, Jiang H, Xie W, Zhang Z, Smrcka AV, Wu D. 2000. Roles of PLC-beta2 and -beta3
882 and PI3Kgamma in chemoattractant-mediated signal transduction. *Science*
883 **287**:1046–1049. doi:10.1126/science.287.5455.1046
884 Liu X, Zhou Q, Hart JR, Xu Y, Yang S, Yang D, Vogt PK, Wang M-W. 2022. Cryo-EM
885 structures of cancer-specific helical and kinase domain mutations of PI3Kα. *Proc*
886 *Natl Acad Sci U S A* **119**:e2215621119. doi:10.1073/pnas.2215621119
887 Lucas CL, Kuehn HS, Zhao F, Niemela JE, Deenick EK, Palendira U, Avery DT, Moens
888 L, Cannons JL, Biancalana M, Stoddard J, Ouyang W, Frucht DM, Rao VK,
889 Atkinson TP, Agharahimi A, Hussey AA, Folio LR, Olivier KN, Fleisher TA,
890 Pittaluga S, Holland SM, Cohen JI, Oliveira JB, Tangye SG, Schwartzberg PL,
891 Lenardo MJ, Uzel G. 2014. Dominant-activating germline mutations in the gene
892 encoding the PI(3)K catalytic subunit p110δ result in T cell senescence and
893 human immunodeficiency. *Nat Immunol* **15**:88–97. doi:10.1038/ni.2771
894 Luo L, Wall AA, Tong SJ, Hung Y, Xiao Z, Tarique AA, Sly PD, Fantino E, Marzolo M-P,
895 Stow JL. 2018. TLR Crosstalk Activates LRP1 to Recruit Rab8a and PI3Kγ for

896 Suppression of Inflammatory Responses. *Cell Rep* **24**:3033–3044.
897 doi:10.1016/j.celrep.2018.08.028
898 Mandelker D, Gabelli SB, Schmidt-Kittler O, Zhu J, Cheong I, Huang C-H, Kinzler KW,
899 Vogelstein B, Amzel LM. 2009. A frequent kinase domain mutation that changes
900 the interaction between PI3Kalpha and the membrane. *Proc Natl Acad Sci USA*
901 **106**:16996–17001. doi:10.1073/pnas.0908444106
902 Masson GR, Burke JE, Ahn NG, Anand GS, Borchers C, Brier S, Bou-Assaf GM, Engen
903 JR, Englander SW, Faber J, Garlish R, Griffin PR, Gross ML, Guttman M,
904 Hamuro Y, Heck AJR, Houde D, Iacob RE, Jørgensen TJD, Kaltashov IA,
905 Klinman JP, Konermann L, Man P, Mayne L, Pascal BD, Reichmann D, Skehel
906 M, Snijder J, Strutzenberg TS, Underbakke ES, Wagner C, Wales TE, Walters
907 BT, Weis DD, Wilson DJ, Wintrode PL, Zhang Z, Zheng J, Schriemer DC, Rand
908 KD. 2019. Recommendations for performing, interpreting and reporting hydrogen
909 deuterium exchange mass spectrometry (HDX-MS) experiments. *Nat Methods*
910 **16**:595–602. doi:10.1038/s41592-019-0459-y
911 Miled N, Yan Y, Hon W-C, Perisic O, Zvelebil M, Inbar Y, Schneidman-Duhovny D,
912 Wolfson HJ, Backer JM, Williams RL. 2007. Mechanism of two classes of cancer
913 mutations in the phosphoinositide 3-kinase catalytic subunit. *Science* **317**:239–
914 242. doi:10.1126/science.1135394
915 Mirdita M, Schütze K, Moriwaki Y, Heo L, Ovchinnikov S, Steinegger M. 2022.
916 ColabFold: making protein folding accessible to all. *Nat Methods* **19**:679–682.
917 doi:10.1038/s41592-022-01488-1
918 Okkenhaug K. 2013. Signaling by the phosphoinositide 3-kinase family in immune cells.
919 *Annu Rev Immunol* **31**:675–704. doi:10.1146/annurev-immunol-032712-095946
920 Pacold ME, Suire S, Perisic O, Lara-Gonzalez S, Davis CT, Walker EH, Hawkins PT,
921 Stephens L, Eccleston JF, Williams RL. 2000. Crystal structure and functional
922 analysis of Ras binding to its effector phosphoinositide 3-kinase gamma. *Cell*
923 **103**:931–943.
924 Perez-Riverol Y, Bai J, Bandla C, García-Seisdedos D, Hewapathirana S,
925 Kamatchinathan S, Kundu DJ, Prakash A, Frericks-Zipper A, Eisenacher M,
926 Walzer M, Wang S, Brazma A, Vizcaíno JA. 2022. The PRIDE database
927 resources in 2022: a hub for mass spectrometry-based proteomics evidences.
928 *Nucleic Acids Res* **50**:D543–D552. doi:10.1093/nar/gkab1038
929 Perino A, Ghigo A, Ferrero E, Morello F, Santulli G, Baillie GS, Damilano F, Dunlop AJ,
930 Pawson C, Walser R, Levi R, Altruda F, Silengo L, Langeberg LK, Neubauer G,
931 Heymans S, Lembo G, Wymann MP, Wetzker R, Houslay MD, Iaccarino G, Scott
932 JD, Hirsch E. 2011. Integrating Cardiac PIP(3) and cAMP Signaling through a
933 PKA Anchoring Function of p110gamma. *Mol Cell* **42**:84–95.
934 doi:10.1016/j.molcel.2011.01.030
935 Pettersen EF, Goddard TD, Huang CC, Couch GS, Greenblatt DM, Meng EC, Ferrin
936 TE. 2004. UCSF Chimera--a visualization system for exploratory research and
937 analysis. *J Comput Chem* **25**:1605–1612. doi:10.1002/jcc.20084

938 Punjani A, Rubinstein JL, Fleet DJ, Brubaker MA. 2017. cryoSPARC: algorithms for
939 rapid unsupervised cryo-EM structure determination. *Nat Methods* **14**:290–296.
940 doi:10.1038/nmeth.4169
941 Rathinaswamy MK, Burke JE. 2019. Class I phosphoinositide 3-kinase (PI3K)
942 regulatory subunits and their roles in signaling and disease. *Adv Biol Regul*
943 100657. doi:10.1016/j.jbior.2019.100657
944 Rathinaswamy MK, Dalwadi U, Fleming KD, Adams C, Stariha JTB, Pardon E, Baek M,
945 Vadas O, DiMaio F, Steyaert J, Hansen SD, Yip CK, Burke JE. 2021a. Structure
946 of the phosphoinositide 3-kinase (PI3K) p110γ-p101 complex reveals molecular
947 mechanism of GPCR activation. *Sci Adv* **7**:eabj4282. doi:10.1126/sciadv.abj4282
948 Rathinaswamy MK, Fleming KD, Dalwadi U, Pardon E, Harris NJ, Yip CK, Steyaert J,
949 Burke JE. 2021b. HDX-MS-optimized approach to characterize nanobodies as
950 tools for biochemical and structural studies of class IB phosphoinositide 3-
951 kinases. *Structure* **29**:1371-1381.e6. doi:10.1016/j.str.2021.07.002
952 Rathinaswamy MK, Gaieb Z, Fleming KD, Borsari C, Harris NJ, Moeller BE, Wymann
953 MP, Amaro RE, Burke JE. 2021c. Disease-related mutations in PI3Kγ disrupt
954 regulatory C-terminal dynamics and reveal a path to selective inhibitors. *Elife*
955 **10**:e64691. doi:10.7554/eLife.64691
956 Rathinaswamy MK, Jenkins ML, Duewell BR, Zhang X, Harris NJ, Evans JT, Stariha
957 JTB, Dalwadi U, Fleming KD, Ranga-Prasad H, Yip CK, Williams RL, Hansen
958 SD, Burke JE. 2023. Molecular basis for differential activation of p101 and p84
959 complexes of PI3Kγ by Ras and GPCRs. *Cell Rep* **42**:112172.
960 doi:10.1016/j.celrep.2023.112172
961 Rynkiewicz NK, Anderson KE, Suire S, Collins DM, Karanasios E, Vadas O, Williams R,
962 Oxley D, Clark J, Stephens LR, Hawkins PT. 2020. Gβγ is a direct regulator of
963 endogenous p101/p110γ and p84/p110γ PI3Kγ complexes in mouse neutrophils.
964 *Sci Signal* **13**:eaaz4003. doi:10.1126/scisignal.aaz4003
965 Samuels Y, Wang Z, Bardelli A, Silliman N, Ptak J, Szabo S, Yan H, Gazdar A, Powell
966 S, Riggins G, Willson J, Markowitz S, Kinzler K, Vogelstein B, Velculescu V.
967 2004. High frequency of mutations of the PIK3CA gene in human cancers.
968 *Science* **304**:554. doi:10.1126/science.1096502
969 Shymanets A, Prajwal P, Bucher K, Beer-Hammer S, Harteneck C, Nürnberg B. 2013.
970 p87 and p101 subunits are distinct regulators determining class IB PI3K
971 specificity. *J Biol Chem* **288(43)**:31059–68. doi:10.1074/jbc.M113.508234
972 Siempelkamp BD, Rathinaswamy MK, Jenkins ML, Burke JE. 2017. Molecular
973 mechanism of activation of class IA phosphoinositide 3-kinases (PI3Ks) by
974 membrane-localized HRas. *J Biol Chem* **292**:12256–12266.
975 doi:10.1074/jbc.M117.789263
976 Stephens LR, Eguinoa A, Erdjument-Bromage H, Lui M, Cooke F, Coadwell J, Smrcka
977 AS, Thelen M, Cadwallader K, Tempst P, Hawkins PT. 1997. The Gbg sensitivity
978 of a PI3K is dependent upon a tightly associated adaptor, p101. *Cell* **89**:105–114.
979 Takeda AJ, Maher TJ, Zhang Y, Lanahan SM, Bucklin ML, Compton SR, Tyler PM,
980 Comrie WA, Matsuda M, Olivier KN, Pittaluga S, McElwee JJ, Long Priel DA,
981 Kuhns DB, Williams RL, Mustillo PJ, Wymann MP, Koneti Rao V, Lucas CL.

982 2019. Human PI3Kγ deficiency and its microbiota-dependent mouse model
983 reveal immunodeficiency and tissue immunopathology. *Nat Commun* **10**:4364–
984 12. doi:10.1038/s41467-019-12311-5
985 Vadas O, Dbouk HA, Shymanets A, Perisic O, Burke JE, Abi Saab WF, Khalil BD,
986 Harteneck C, Bresnick AR, Nürnberg B, Backer JM, Williams RL. 2013.
987 Molecular determinants of PI3Kγ-mediated activation downstream of G-protein-
988 coupled receptors (GPCRs). *Proc Natl Acad Sci U S A* **110**:18862–18867.
989 doi:10.1073/pnas.1304801110
990 Vanhaesebroeck B, Perry MWD, Brown JR, André F, Okkenhaug K. 2021. PI3K
991 inhibitors are finally coming of age. *Nat Rev Drug Discov* **20**:741–769.
992 doi:10.1038/s41573-021-00209-1
993 Vasan N, Cantley LC. 2022. At a crossroads: how to translate the roles of PI3K in
994 oncogenic and metabolic signalling into improvements in cancer therapy. *Nat*
995 *Rev Clin Oncol*. doi:10.1038/s41571-022-00633-1
996 Walker EH, Perisic O, Ried C, Stephens L, Williams RL. 1999. Structural insights into
997 phosphoinositide 3-kinase catalysis and signalling. *Nature* **402**:313–320.
998 doi:10.1038/46319
999 Walser R, Burke JE, Gogvadze E, Bohnacker T, Zhang X, Hess D, Küenzi P, Leitges M,
1000 Hirsch E, Williams RL, Laffargue M, Wymann MP. 2013. PKCβ phosphorylates
1001 PI3Kγ to activate it and release it from GPCR control. *PLoS Biol* **11**:e1001587.
1002 doi:10.1371/journal.pbio.1001587
1003 Zhang X, Vadas O, Perisic O, Anderson KE, Clark J, Hawkins PT, Stephens LR,
1004 Williams RL. 2011. Structure of lipid kinase p110β/p85β elucidates an unusual
1005 SH2-domain-mediated inhibitory mechanism. *Mol Cell* **41**:567–578.
1006 doi:10.1016/j.molcel.2011.01.026
1007
1008
1009
1010
1011
1012
1013
1014
1015
1016
1017
1018
1019

1020 ## Figures and Figure Legends

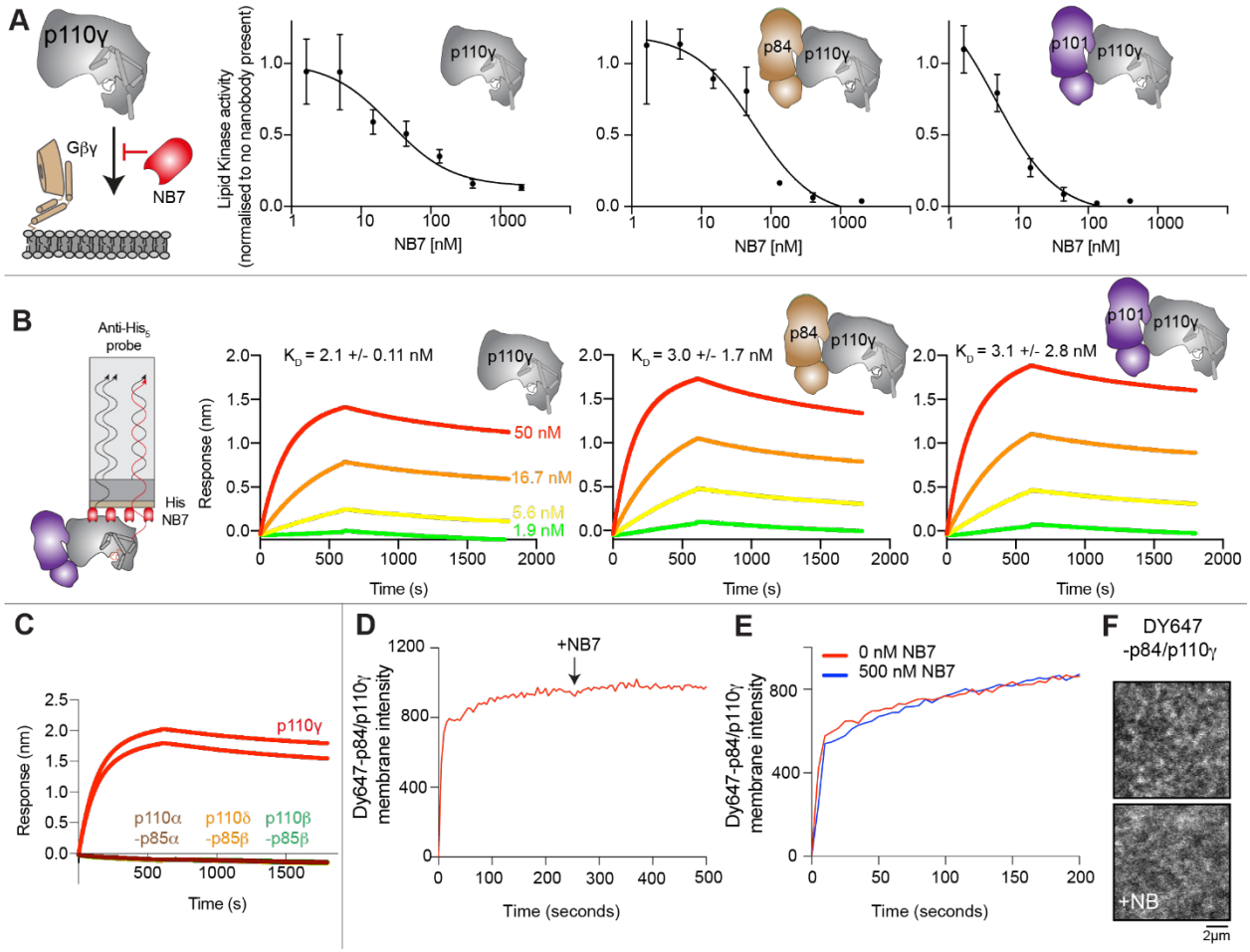

1021

1022 **Figure 1. The inhibitory nanobody NB7 binds tightly to all p110γ complexes and inhibits kinase**
1023 **activity, but does not prevent membrane binding**

1024 **A.** Cartoon schematic depicting nanobody inhibition of activation by lipidated Gβγ (1.5 μM final
1025 concentration). Lipid kinase assays show a potent inhibition of lipid kinase activity with increasing
1026 concentrations of NB7 (3-3000 nM) for the different complexes. The protein concentration of p110γ (300
1027 nM), p110γ-p84 (330 nM) and p110γ-p101 (12 nM) was different due to intrinsic differences of each
1028 complex to be activated by lipidated Gβγ.

1029 **B**. Association and dissociation curves for the dose response of His-NB7 binding to p110γ, p110γ-p84
1030 and p110γ-p101 (50 – 1.9 nM) is shown. A cartoon schematic of BLI analysis of the binding of
1031 immobilized His-NB7 to p110γ is shown on the left. Dissociation constants (K_D) were calculated based on
1032 a global fit to a 1:1 model for the top three concentrations and averaged with error shown.

1033 **B**. Association and dissociation curves for His-NB7 binding to p110γ, p110α-p85α, p110β-p85β, and
1034 p110δ-p85β. Experiments were performed in duplicate with a final concentration of 50 nM of each class I
1035 PI3K complex.
1036 **D**. Total Internal Reflection Fluorescence Microscopy (TIRF-M) analysis of the effect of nanobody NB7 on
1037 PI3K recruitment to supported lipid bilayers containing H-Ras(GTP) and farnesyl-Gβγ. Y647-p84/p110γ
1038 displays rapid equilibration kinetics and is insensitive to the addition of 500 nM nanobody (black arrow,
1039 250 sec) on supported lipid bilayers containing H-Ras(GTP) and farnesyl-Gβγ.
1040 **E**. Kinetics of 50 nM DY647-p84/p110γ membrane recruitment appears indistinguishable in the absence
1041 and presence of nanobody. Prior to sample injection, DY647-p84/p110γ was incubated for 10 minutes
1042 with 500 nM nanobody.
1043 **F**. Representative TIRF-M images showing the localization of 50 nM DY647-p84/p110γ visualized in the
1044 absence or presence of 500 nM nanobody (+NB7). Membrane composition for panels C-E: 93% DOPC,
1045 5% DOPS, 2% MCC-PE, Ras(GTP) covalently attached to MCC-PE, and 200 nM farnesyl-Gβγ.
1046
1047
1048
1049
1050
1051
1052
1053
1054
1055
1056
1057
1058
1059

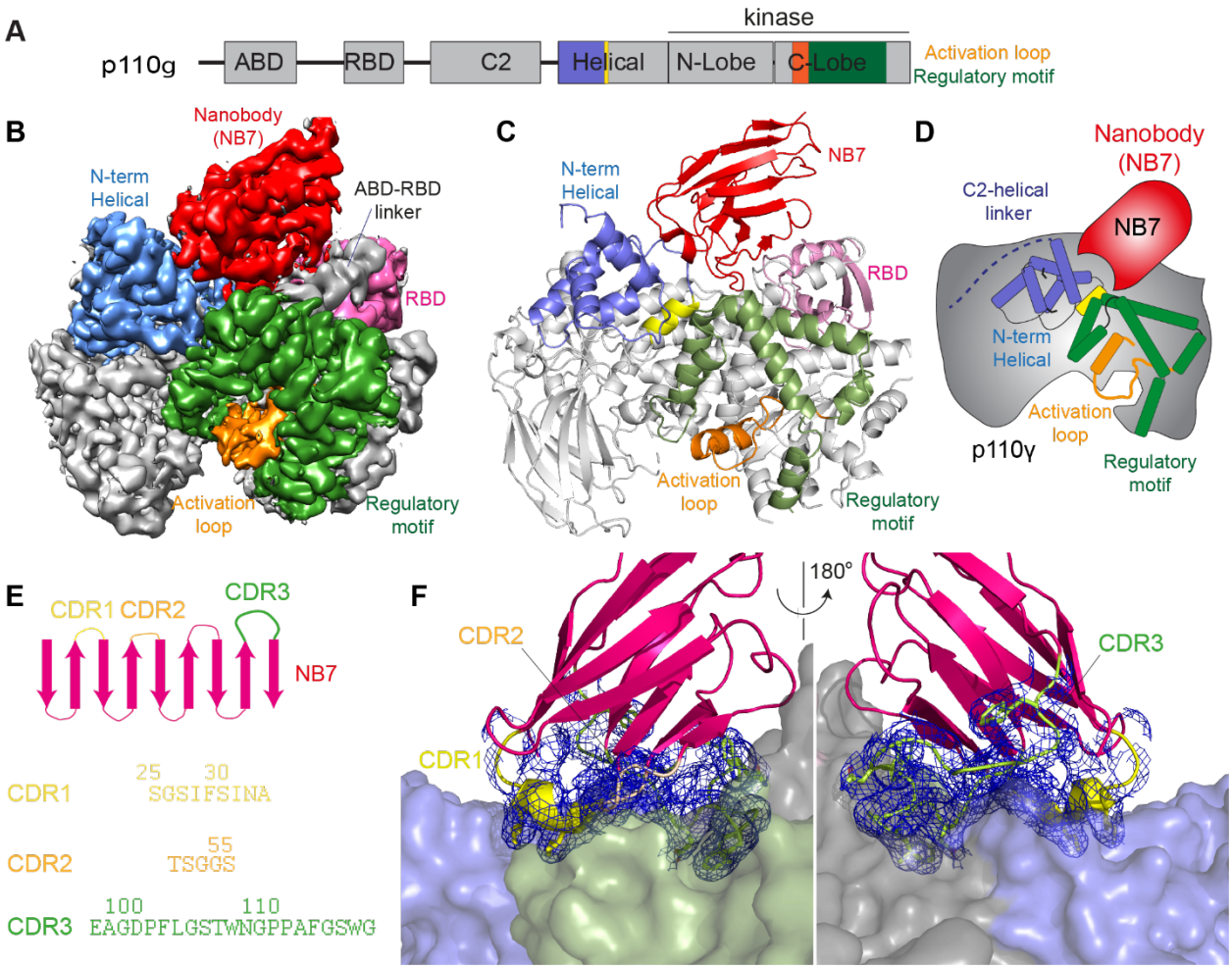

Figure 2. Structure of p110γ bound to inhibitory nanobody NB7

A. Domain schematics of p110γ with helical domain (blue), activation loop (orange), and regulatory motif (green) of p110 annotated.

B. Density map of the p110γ-NB7 complex colored according to the schematic in **A**.

C. Cartoon model of the structure of p110γ bound to NB7 colored according to **A**.

D. Schematic depicting the key features of p110 and the nanobody binding site, colored according to panel **A**.

E. Domain schematic of NB7 CDR regions and their sequences.

F. Zoom in on the binding interface of NB7, with the CDRs colored as in panel E, and the electron density of the CDR regions contoured at 3σ (blue mesh).

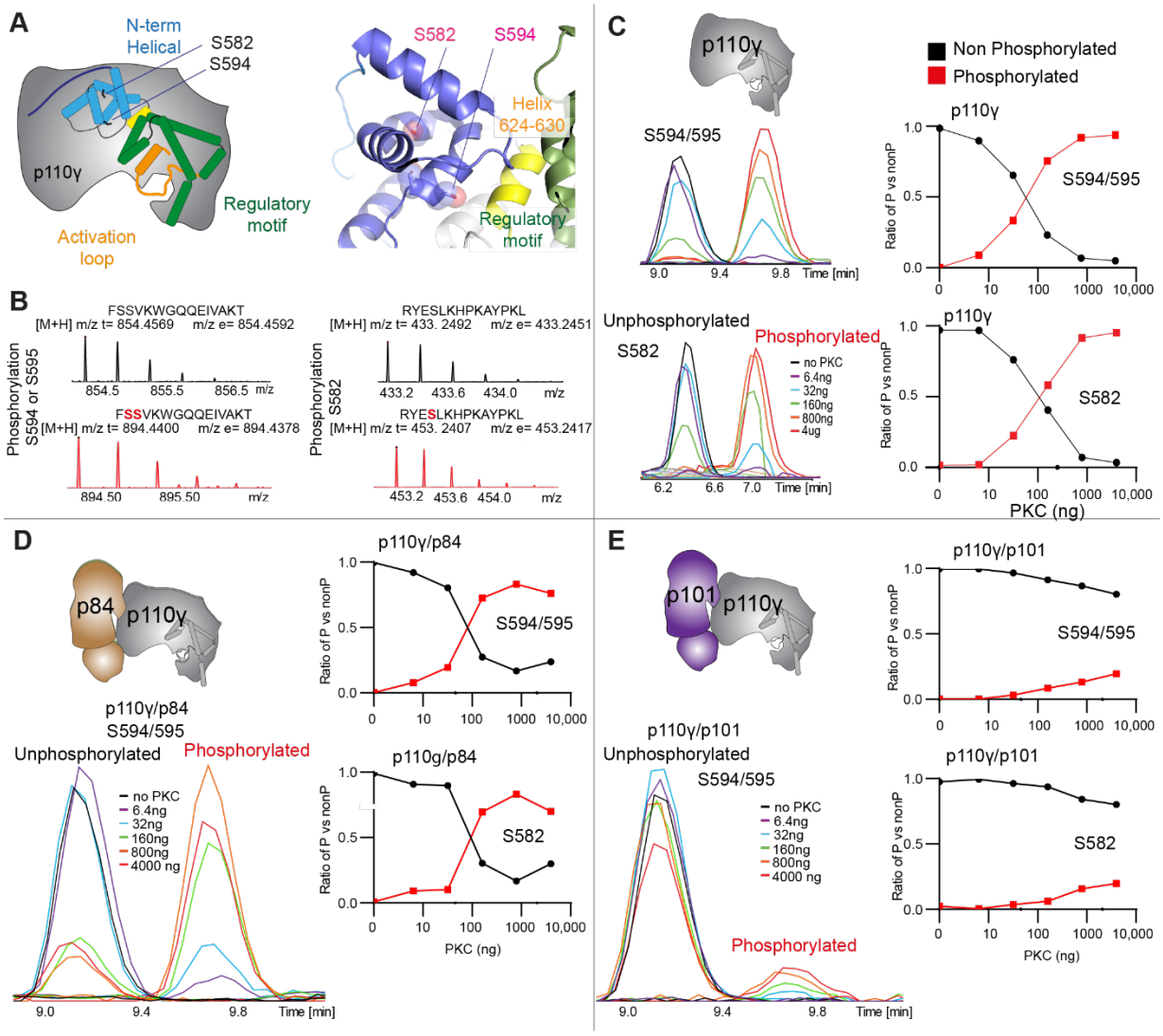

Figure 3. PKC leads to dual phosphorylation of internal sites in the helical domain, with selectivity for apo p110γ and p110γ-p84 over p110γ-p101.

A. Putative phosphorylation sites mapped on the structure of p110γ (PDB: 7MEZ) and cartoon schematic. The regions are colored based on domain schematics featured in Fig 2A.

B. Raw MS spectra of the unphosphorylated and phosphorylated peptide for a region spanning 579-592 (RYESLKHPKAYPKL) and 593-607 (FSSVKWGQQEIVAKT).

C-E. Extracted traces and ratios of the intensity of extracted ion traces of different phosphorylation site peptides (Top to bottom: S594/S595 and S582) from © p110γ, (**D**) p110γ/p84 or **(E**) p110γ/p101 samples treated with increasing concentration of PKCb according to the legend.

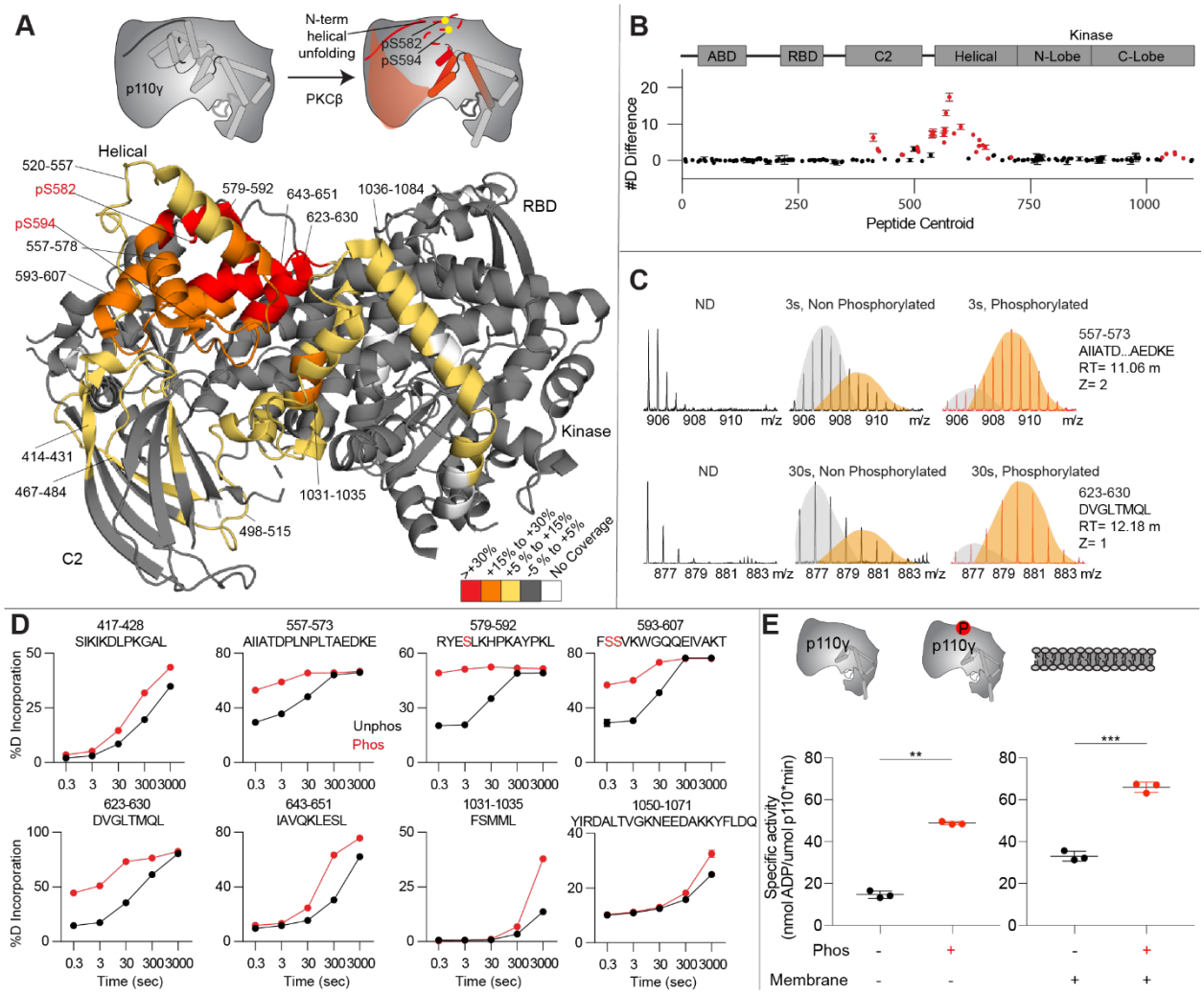

Figure 4. Activating phosphorylation at the helical domain leads to opening of the regulatory motif

A. HDX-MS comparing apo and phosphorylated p110γ. Significant differences in deuterium exchange are mapped on to the structure and cartoon of p110γ according to the legend (PDB: 7MEZ).

B. The graph of the #D difference in deuterium incorporation for p110γ, with each point representing a single peptide. Peptides colored in red are those that had a significant change in the mutants (greater than 0.4 Da and 5% difference at any timepoint, with a two tailed t-test p<0.01). Error bars are S.D. (n=3).

C. Representative bimodal distribution (EX1 kinetics) observed in the helical domain peptides of p110γ.

D. Representative p100γ peptides displaying increases in exchange in the phosphorylated state are shown. For all panels, error bars show SD (n=3)

E. Lipid kinase activity assays of phosphorylated and non-phosphorylated p100γ (concentration, 12nM to 1000nM) ATPase activity (left) and membrane (5% phosphatidylinositol 4,5-bisphosphate (PIP2), 95% phosphatidylserine (PS)) activation (right). Significance is indicated by **(<0.001%), and ***(<0.0001%).

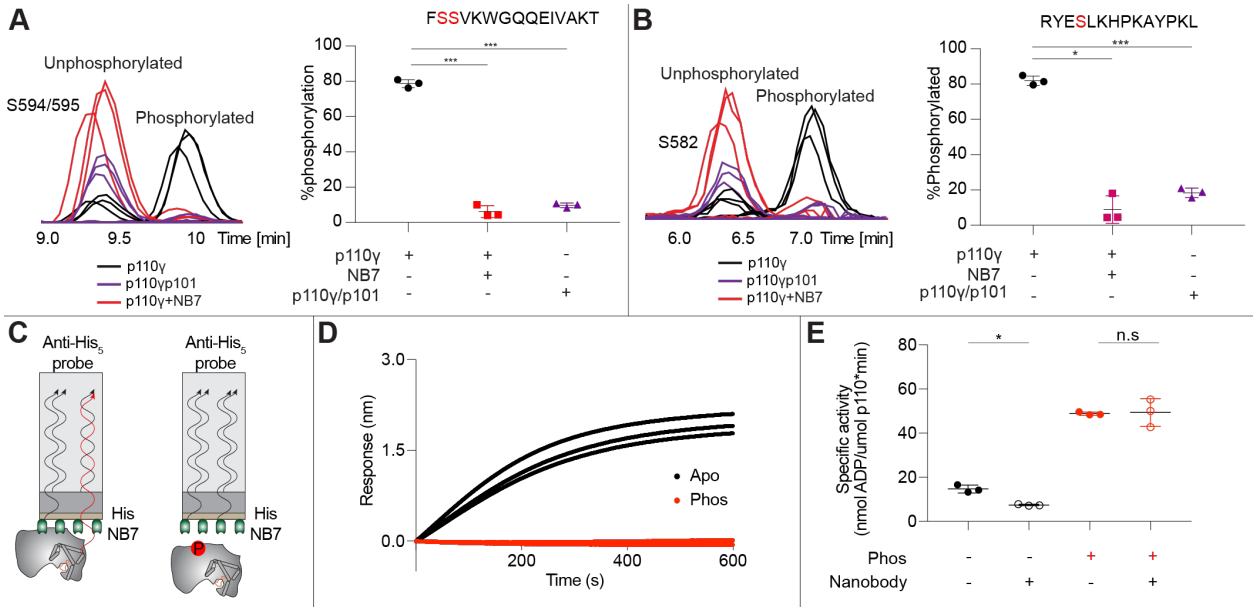

Figure 5. Nanobody NB7 blocks PKC phosphorylation, and phosphorylation prevents nanobody binding.

A. Graph showing the intensities of phosphorylated and non-phosphorylated p110γ peptide (593-607) for PKC (500 nM) treated p110γ (black), PKC treated p110γ with NB7 (red) and PKC treated p110γp101 (purple). Scatter plot showing the percent phosphorylation of each complex from the left graph for the indicated peptide (n=3, right). Significance is indicated by ***(<0.0001%).

B. Graph showing the intensities of phosphorylated and non-phosphorylated p110γ peptide (579-592) for PKC treated p110γ (black), PKC treated p110γ with NB7 (red) and PKC treated p110γp101 (purple). Scatter plot showing the percent phosphorylation of each complex from the left graph for the indicated peptide (n=3, right). Significance is indicated by * (<0.01%), and ***(<0.0001%).

C. Cartoon schematic of BLI analysis of the binding of immobilized His-NB7 to phosphorylated and non-phosphorylated p110γ.

D. Association curves for phosphorylated and non-phosphorylated p110γ (25nM) binding to His-NB7 are shown (n=3).

E. Kinase activity assays comparing the activation/inhibition of phosphorylated and non-phosphorylated p110γ (concentration, 12nM to 1000nM) with or without nanobody (3000nM final). Significance is indicated by * (<0.05%), and NS (>0.05%).

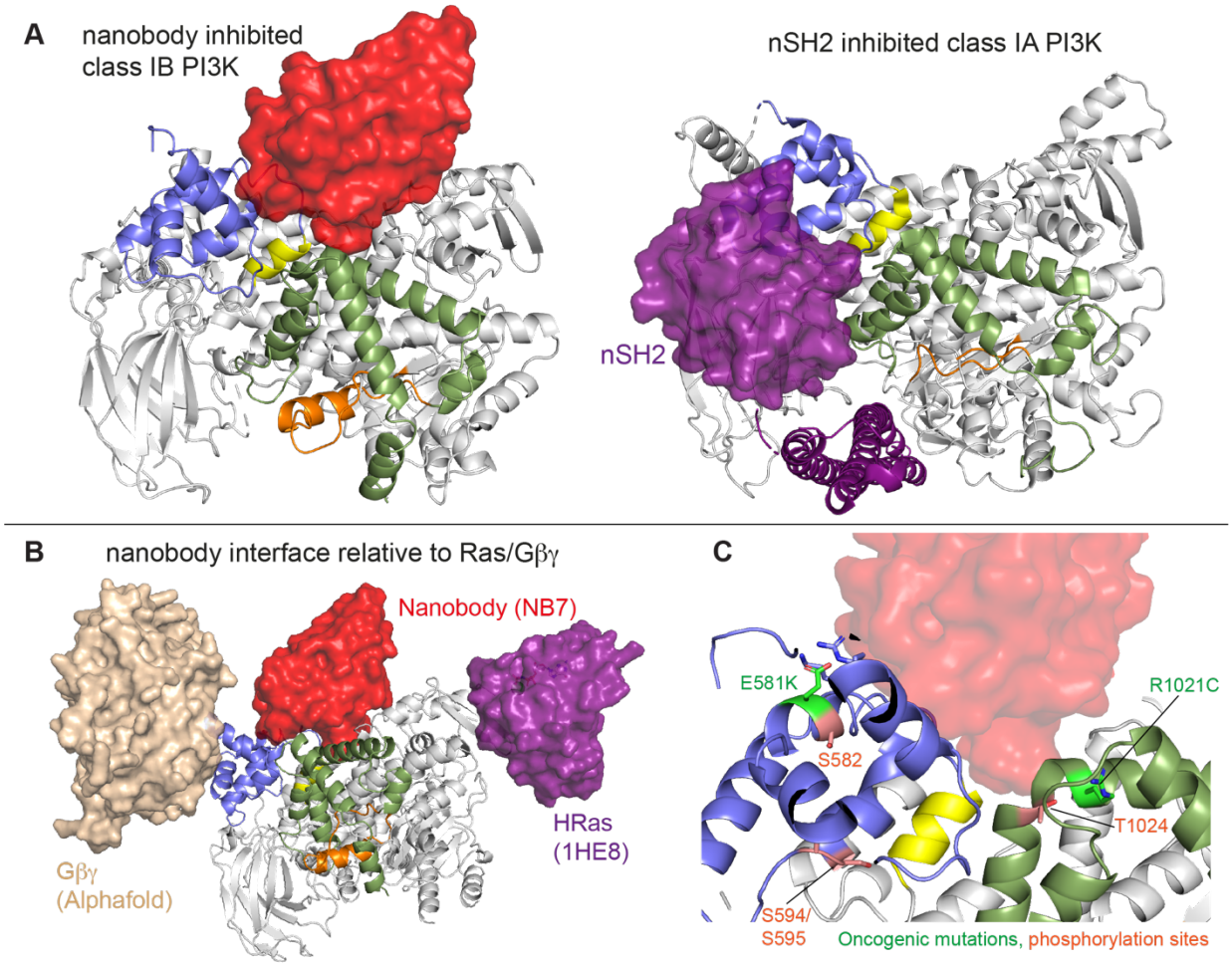

Figure 6. Comparison of nanobody binding site compared to p85 inhibition of class IA PI3Ks and class IB activation sites

A. Comparison of the nanobody NB7 binding site in p110γ compared to the nSH2 inhibitory site in p110α (PDB: 3HHM) (Mandelker et al., 2009)

B. Comparison of the nanobody NB7 binding site in p110γ compared to the X-ray structure of the Ras binding site (PDB: 1HE8) (Pacold et al., 2000) and the Alphafold model of Gβγ bound to p110γ (Rathinaswamy et al., 2023).

C. Oncogenic mutations and post-translational modifications in spatial proximity to the nanobody binding site.

1132 **Supplemental information for:**

1133

1134 Allosteric activation or inhibition of PI3Kγ mediated through 1135 conformational changes in the p110γ helical domain

1136

1137 Noah J Harris[1*], Meredith L Jenkins[1*], Sung-Eun Nam, Manoj K Rathinaswamy[1],
1138 Matthew Parson[1], Harish Ranga-Prasad[1], Udit Dalwadi[2], Brandon E Moeller[1], Eleanor
1139 Sheekey[1], Scott D Hansen[3], Calvin K Yip[2%], and John E Burke[1,2%]

1140

1141

1142 [1]Department of Biochemistry and Microbiology, University of Victoria, Victoria, British
1143 Columbia, V8W 2Y2, Canada
1144 [2]Department of Biochemistry and Molecular Biology, The University of British Columbia,
1145 Vancouver, British Columbia V6T 1Z3, Canada
1146 [3]Institute of Molecular Biology, University of Oregon, Eugene, OR 97403

1147

1148 *These authors contributed equally
1149 [%]To whom correspondence should be addressed: John E. Burke
1150 Tel: 1-250-721-8732, email: jeburke@uvic.ca
1151 Calvin K Yip
1152 Tel: 1-604-827-3976, em ail: calvin.yip@ubc.ca

1153
1154
1155
1156
1157
1158
1159
1160
1161
1162
1163

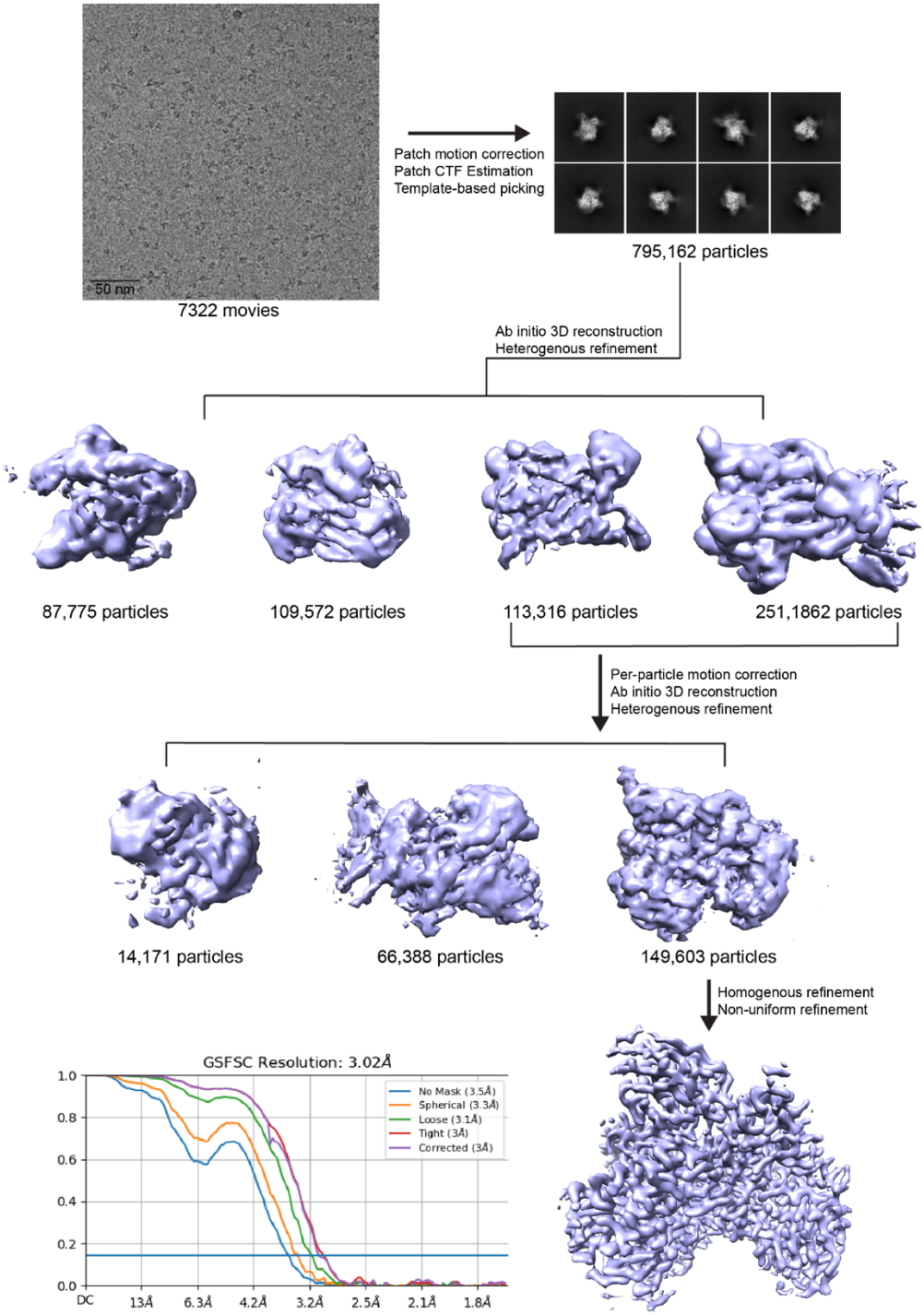

Figure S1. p110γ-NB7 complex cryo-EM analysis workflow (related to main figure 2): cryo-EM processing workflow of p110γ-NB7 complex are shown in order of a representative micrographs, representative 2D classification and 3D reconstruction processing strategy. Bottom left shows Gold-standard Fourier shell Correlation (FSC) curve of final round on non-uniform homogenous refinement.

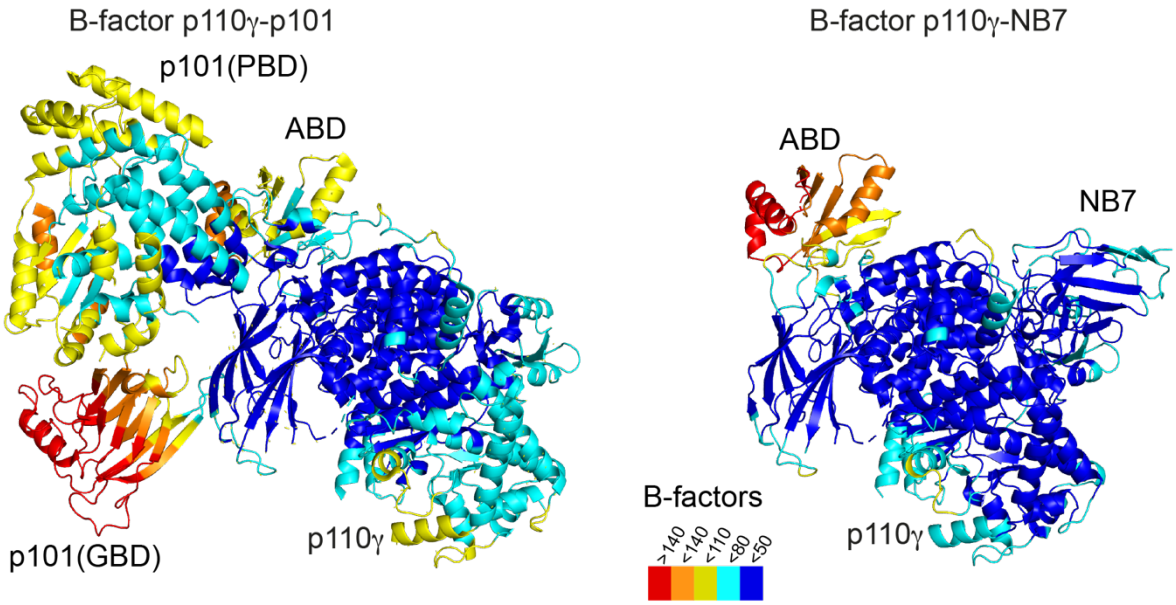

Figure S2. Comparison of full length p110γ bound to NB7 compared to p110γ-p101 (related to main figure 2): The structure of the p110γ-p101 complex (PDB:7MEZ) compared to the NB7-p110γ complex is shown colored according to B factor based on the legend.

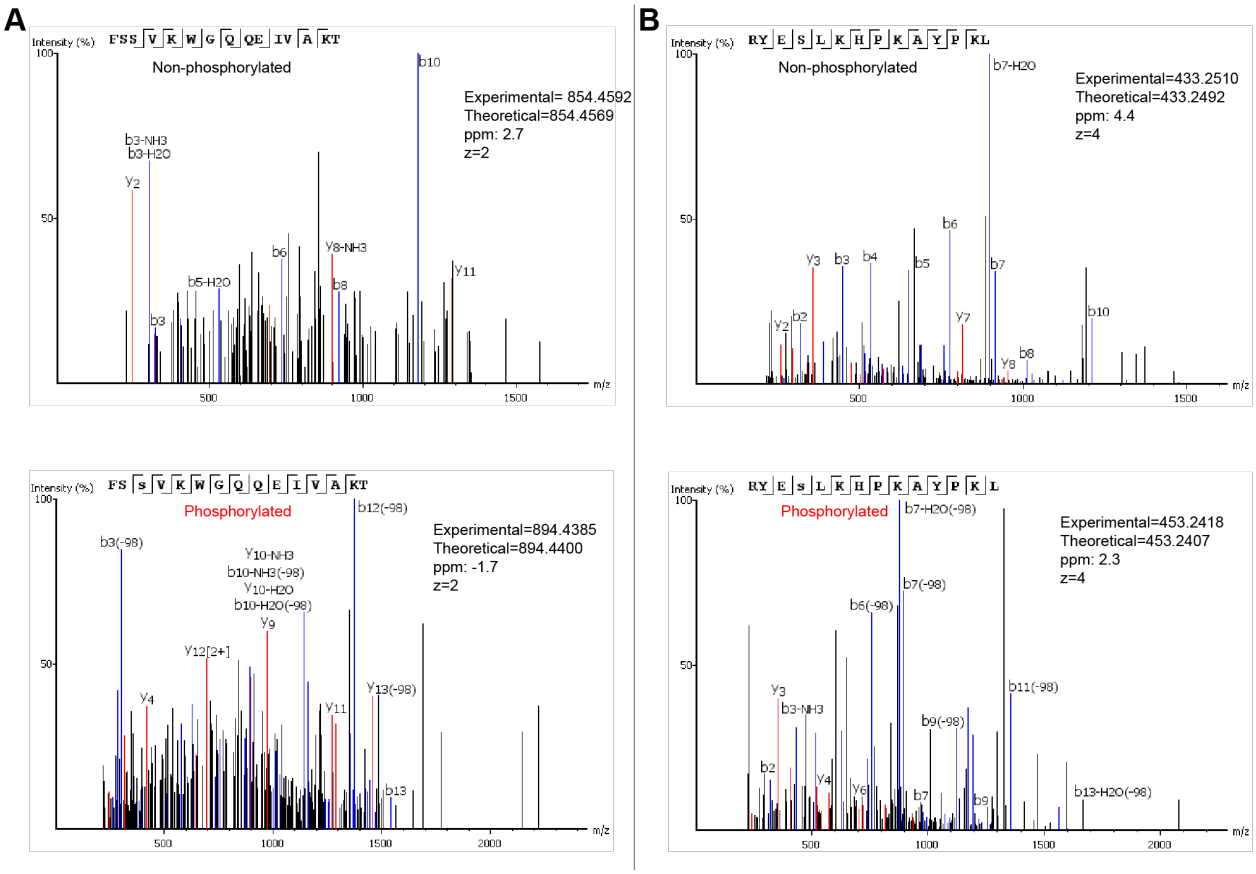

Figure S3 (related to main figure 3). MS/MS spectra of peptides spanning S582 and S594/S595 for both phosphorylated and unphosphorylated states. The theoretical and experimental mass are annotated for all peptides.

1195

1196 **Supplementary table 1.** Cryo-EM data collection, refinement and validation statistics

1197 **(related to main figure 2)**

	p110γ-NB7 EMD- 27627 PDB: 8DP0
Data collection and processing	
Magnification	
Voltage (kV)	300
Electron exposure (e/ Å^2)	50
Defocus range (nM)	500-2500
Pixel size (Å)	
Symmetry imposed	C1
Initial particle images (no.)	795,162
Final particle images (no.)	149,603
Map resolution (Å)	3.02
FSC threshold	0.143
Map resolution range (Å)	2.6-4.4
Refinement	
Initial model used (PDB)	7MEZ (p110γ only)
Model Resolution (Å)	3.02
FSC threshold	0.5
Map sharpening B factor	Sharpened locally
Model composition	
Non-hydrogen atoms	8737
Protein residues	1,066
Ligands	0
B-factors	
Protein	52.4
Validation	
Mol probability score	1.29
Clashscore	5.33
Poor rotamers (%)	0.0
Ramachandran	
Favored	98.41
Allowed	1.59
Outliers	0.0
R.m.s. deviations	
Bond lengths (Å)	0.002
Bond angles (°)	0.490
Model to map fit (CC_mask)	0.86

1198

1199

1200

1201

1202

1203
1204
1205 **Supplementary table 2.** HDX-MS data collection and validation statistics
1206 **(related to main figure 4)**

Data set	p110γ unphosphorylated	p110γ phosphorylated
HDX reaction details	%D_2O=75.5% $pH_{(read)}$=7.5 Temp=4ºC, 20ºC	%D_2O=75.5% pH(read)=7.5 Temp=4ºC, 20ºC
HDX time course (seconds)	3s at 4ºC, 3s, 30s, 300s, 3000s at 20 ºC	3s at 4ºC, 3s, 30s, 300s, 3000s at 20 ºC
HDX controls	N/A	N/A
Back-exchange	No correction, deuterium levels are relative	No correction, deuterium levels are relative
Number of peptides	244	244
Sequence coverage	98.4%	98.4%
Average peptide /redundancy	Length= 15.2 Redundancy= 3.3	Length= 15.2 Redundancy= 3.3
Replicates	3	3
Repeatability	Average StDev=0.53%	Average StDev=0.57%
Significant differences in HDX	>5% and >0.4 Da and unpaired t-test ≤0.01	>5% and >0.4 Da and unpaired t-test ≤0.01

1207